A discontinuous Galerkin formulation for nonlinear analysis of multilayered shells refined theories

Giuliano Guarino[a], Alberto Milazzo[a,*]

[a]*Department of Engineering, University of Palermo, Viale delle Scienze, Bld. 8, Palermo, 90128, Italy.*

Abstract

A novel pure penalty discontinuous Galerkin method is proposed for the geometrically nonlinear analysis of multilayered composite plates and shells, modelled via high-order refined theories. The approach allows to build different two-dimensional equivalent single layer structural models, which are obtained by expressing the covariant components of the displacement field through-the-thickness via Taylor's polynomial expansion of different order. The problem governing equations are deduced starting from the geometrically nonlinear principle of virtual displacements in a total Lagrangian formulation. They are addressed with a pure penalty discontinuous Galerkin method using Legendre polynomials trial functions. The resulting nonlinear algebraic system is solved by a Newton-Raphson arc-length linearization scheme. Numerical tests involving plates and shells are proposed to validate the method, by comparison with literature benchmark problems and finite element solutions, and to assess its features. The obtained results demonstrate the accuracy of the method as well as the effectiveness of high-order elements.

Keywords: Multilayered shells, geometrical nonlinearity, discontinuous Galerkin method, high-order modelling

*Corresponding author
Email addresses: giuliano.guarino@unipa.it (Giuliano Guarino), alberto.milazzo@unipa.it (Alberto Milazzo)

1. Introduction

Thin-walled multilayered composite components, in the form of plates, shells and their assemblies, are of great interest in structural applications and are widely used to minimize the weight while still being very effective in carrying applied external loads. In particular, shells, which are characterized by a curved mid-surface, offer the designer the possibility to take advantage of the strong coupling between flexural and membrane behaviours; on the other hand, sometimes, the need for a curved surface is due to non-structural requirements, e.g. in aerodynamic components. Generally, thin-walled structures operate in the small displacements regime and the linear elastic analysis may be sufficient to predict their response. However, in advanced applications they may undergo large displacements, requiring non-linear analysis to characterize accurately their behaviour. In this framework, a fundamental role is played by the modelling and analysis of these structure that need to be carried out with appropriate fidelity and cost effectiveness to implement successfully their design and optimization.

Due to their geometric characteristics, plates and shells are generally modelled via two–dimensional (2D) theories, which allow to significantly reduce the computational cost in numerical solutions. Focusing on nonlinear behaviour, the first model was developed by Von Kármán [1] who supplemented with non-linear terms the classical Kirchhoff-Love theory [2]. Afterwards, the First Order Shear Deformation Theory (FSDT) by Reissner [3] and Mindlin [4] introduced the assumption of a constant shear deformation across the thickness extending the accuracy of the model to moderately thick plates and shells. A comprehensive review of the multitude of improvements developed to the above mentioned classical theories can be found in the work by Chia [5]. However, the wide use of multilayered composite plates and shells showed the need of more accurate models based on higher-order assumptions on the behaviour of the kinematic and mechanical

fields throughout the thickness of the structure. Thus, to enhance the modelling accuracy, refined theories have been developed based on high-order expansion of the model primary variables across the thickness. The theories developed can be classified into two categories: *i)* Equivalent-Single-Layer (ESL) approaches that are based on common variable expansions for all the layers of the laminate; *ii)* Layer-Wise (LW) approaches where each layer has its own expansion and only the C_0 continuity of the solution at the elements interface is guaranteed by properly choosing such functions. ESL and LW theories have been unified in the framework of the Carrera Unified Formulation (CUF) [6, 7] that is a powerful technique to develop and implement general plates and shells theories and the related solution numerical tools.

The nonlinear governing equations stemming from plates and shells two–dimensional high-order theories are generally strongly coupled partial differential equations and their solution in close form is very difficult and restricted to simple cases. Thus, numerical methods need to be introduced to solve these structural models and the most common approach in the literature is the finite element method (e.g. Refs. [8, 9, 10, 11, 12]). To cite some amongst the alternatives to finite elements, the Ritz method was recently used to study the buckling and post-buckling behaviour of plates using the FSDT [13, 14, 15, 16, 17, 18] and the third-order shear deformation theory [19, 20]. Mesh-less solutions have been proposed using the smoothed particle hydrodynamics method [21], the mesh-free collocation method [22], the meshless collocation method [23] and the radial basis function method [24]. Also the isogeometric analysis approach (IGA) has been employed to investigate the behaviour of shells using classical theories for both the linear [25, 26] and non-linear regimes [27, 28, 29, 30]; IGA models have been also proposed in combination with high-order theories for linear [31, 32] and non-linear [33] analysis.

The discontinuous Galerkin (dG) method has been recently used for elasticity problem

solutions [34, 35, 36]. It is based on the partition of the problem domain into elements and some penalization integrals to enforce the continuity of the solution across these elements and the boundary conditions. The dG method has interesting advantages in the use of nonstandard element and shape functions, in the application of non conformal meshes as well as high-order elements, in the implementation of meshing strategies such as hierarchical refinement and adaptativity, in scalable implementations and in addressing of locking phenomena. These features can underlie a robust treatment of complex geometries and loadings such as those occurring in advanced lightweight structures. Indeed, the examination of the relevant literature reveals that the dG method attracted interest in this field. In particular, dG formulations and investigations have been proposed for the linear analysis of: *(i)* plates, modelled by the Kircchoff [37, 38, 39] and Mindlin-Reissner [40, 41, 42] first order theories; *(ii)* shells studied by using the Kircchoff-Love [43], Koiter[44] and Reissner-Mindlin [45] first order theories. As regard the non-linear regime, dG methods have been employed for the solution of: *(i)* Kircchoff plates [46, 47, 48], *(ii)* Kircchoff-Love shells[49, 50, 51] and *(iii)* shear flexible shells modelled with the first order theory[52, 53]. Also, refined shell models have been proposed for both the linear [54] and nonlinear [55] analysis, based on finite elements built using a dG approach along the thickness direction. Generally the reported formulations refer to isotropic, homogeneous sections whereas a few works focus on multilayered structures [54, 55, 46]. Eventually, the authors and co-workers proposed dG formulations for high-order theories of multilayered plates [56, 57, 58] and shells [59, 60, 61] addressing linear static and buckling analysis.

In this framework, to the best of the authors' knowledge, the dG method has never been adopted in combination with high-order theories for the nonlinear analysis of plates and shells. This is the main motivation of the present research, which extends previous authors' works [59, 60] where a dG approach is developed for linear behaviour of shells.

Here, for the first time, a discontinuous Galerkin formulation for the geometrically non-linear static analysis of multilayered shells is presented and validated, which is the novelty of the present work.

In the context of a total Lagrangian approach, the proposed formulation provides two-dimensional models of shells assuming the kinematic fields expansion along the thickness up to a desired order and using equivalent single-layer modelization. The resulting governing equations are solved via the dG method based on the pure penalty approach exploring the use of high-order elements, which are expected to present high convergence rates and high level of accuracy with a contained number of degrees of freedom. This has been confirmed by the proposed validation examples, which illustrates the method characteristics.

The paper is organized as following: in Sec.(2) the shell models and the corresponding governing equations in their weak form are deduced for the geometrically non-liner static analysis; Sec.(3) describes the discontinuous Galerkin method used to numerically solve the shell models; in Sec.(4) some benchmark solutions and their comparison with literature or finite element results are presented to validate the approach and assess its features; finally, conclusions are drawn.

2. Shell model

Let us consider a composite, multilayered, generally-curved shell subjected to prescribed external loads and boundary conditions. The shell is built by stacking N_ℓ fiber-reinforced layers, which are modelled as homogeneous and orthotropic and are assumed to be perfectly bonded at their interfaces. A quantity referring to the ℓ-th layer is denoted by a superscript $\langle \ell \rangle$; as such, the volume occupied by the ℓ-th layer is denoted by $V^{\langle \ell \rangle}$ and its fiber deposition angle by $\theta^{\langle \ell \rangle}$. Each layer has uniform thickness $\tau^{\langle \ell \rangle}$ and thus the

thickness of the whole laminate is $\tau = \sum_{\ell=1}^{N_\ell} \tau^{\langle \ell \rangle}$. The volume of the shell $V \subset \mathbb{R}^3$ is obtained as $V = \cup_{\ell=1}^{N_\ell} V^{\langle \ell \rangle}$ and its boundary is denoted as ∂V.

In the following, the Eisntein's summation convention is used with Latin indices i and j taking values in the set $\{1, 2, 3\}$ and Greek indices α and β taking values in the set $\{1, 2\}$.

2.1. Shell geometry

Let the mid-surface of the shell in the undeformed configuration be denoted as $S \subset \mathbb{R}^3$ and let it be described mapping the so-called reference domain $\Omega_\xi \subset \mathbb{R}^2$ (see Fig. 1). The map uses two curvilinear variables ξ_1 and ξ_2 that span in Ω_ξ. Introduced an orthogonal reference system $x_1 x_2 x_3$, a generic point $\boldsymbol{x}_0 = \{x_{01}\ x_{02}\ x_{03}\}^{\mathrm{T}}$ of S is obtained as

$$\boldsymbol{x}_0 = \boldsymbol{x}_0(\xi_1, \xi_2), \quad \text{for } (\xi_1, \xi_2) \in \Omega_\xi. \tag{1}$$

Starting from Eq. (1), for each point on the shell mid-surface, the unit normal vector is defined as

$$\boldsymbol{n}_0 = \frac{\boldsymbol{a}_1 \times \boldsymbol{a}_2}{||\boldsymbol{a}_1 \times \boldsymbol{a}_2||}, \tag{2}$$

where

$$\boldsymbol{a}_i = \frac{\partial \boldsymbol{x}_0}{\partial \xi_i} \qquad i = 1,\ 2 \tag{3}$$

A point $\boldsymbol{x} = \{x_1\ x_2\ x_3\}^{\mathrm{T}}$ in the volume of the shell V has orthogonal coordinates described by the map

$$\boldsymbol{x} = \boldsymbol{x}(\xi_1, \xi_2, \xi_3) = \boldsymbol{x}_0(\xi_1, \xi_2) + \xi_3 \boldsymbol{n}_0(\xi_1, \xi_2), \quad \text{for } (\xi_1, \xi_2, \xi_3) \in \Omega_\xi \times I_{\xi_3}, \tag{4}$$

where the thickness curvilinear coordinate ξ_3 is introduced spanning the set $I_{\xi_3} = [-\tau/2, \tau/2]$. Consistently, the volume of the ℓ-th layer is identified as the region of V where $\xi_3 \in I_{\xi_3}^{\langle \ell \rangle} = [\xi_{3b}^{\langle \ell \rangle}, \xi_{3t}^{\langle \ell \rangle}]$, being $\xi_{3b}^{\langle \ell \rangle}$ and $\xi_{3t}^{\langle \ell \rangle}$ the ξ_3 coordinates of the bottom and top faces of the ℓ-th layer, respectively. As such, it results that $\xi_{3b}^{\langle 1 \rangle} = -\tau/2$, $\xi_{3t}^{\langle N_\ell \rangle} = \tau/2$, $\tau^{\langle \ell \rangle} = \xi_{3t}^{\langle \ell \rangle} - \xi_{3b}^{\langle \ell \rangle}$ and $\xi_{3t}^{\langle \ell - 1 \rangle} = \xi_{3b}^{\langle \ell \rangle}$ for $\ell = 2, ..., N_\ell$. The map of the volume is used to define the vectors $\boldsymbol{g}_i$ of the local covariant basis and the vectors $\boldsymbol{g}^i$ of the local contravariant basis as

$$\boldsymbol{g}_i = \frac{\partial \boldsymbol{x}}{\partial \xi_i} \tag{5a}$$

$$\boldsymbol{g}^i \cdot \boldsymbol{g}_j = \delta_i^j, \tag{5b}$$

where δ_i^j is the Kronecker delta. Additionally, the ij-th covariant and contravariant components of the metric tensor are obtained as $g_{ij} = \boldsymbol{g}_i \cdot \boldsymbol{g}_j$ and $g^{ij} = \boldsymbol{g}^i \cdot \boldsymbol{g}^j$, respectively.

Eventually, to the aim of the formulation development, it is worth noting that a vector in $\mathbb{R}^3$ is either described in terms of its components in the orthogonal reference system as $\boldsymbol{v} = \{v_1 \ v_2 \ v_3\}^{\mathrm{T}}$ or in terms of its covariant components as $\boldsymbol{v}_\xi = \{v_{\xi_1} \ v_{\xi_2} \ v_{\xi_3}\}^{\mathrm{T}}$. These vectors obey the following transformation law

$$\boldsymbol{v} = \boldsymbol{R}_\xi \boldsymbol{v}_\xi. \tag{6}$$

where the matrix $\boldsymbol{R}_\xi$ collects the contravariant basis as columns. For more details on the differential geometry employed in the present work, the interested reader is referred to [62].

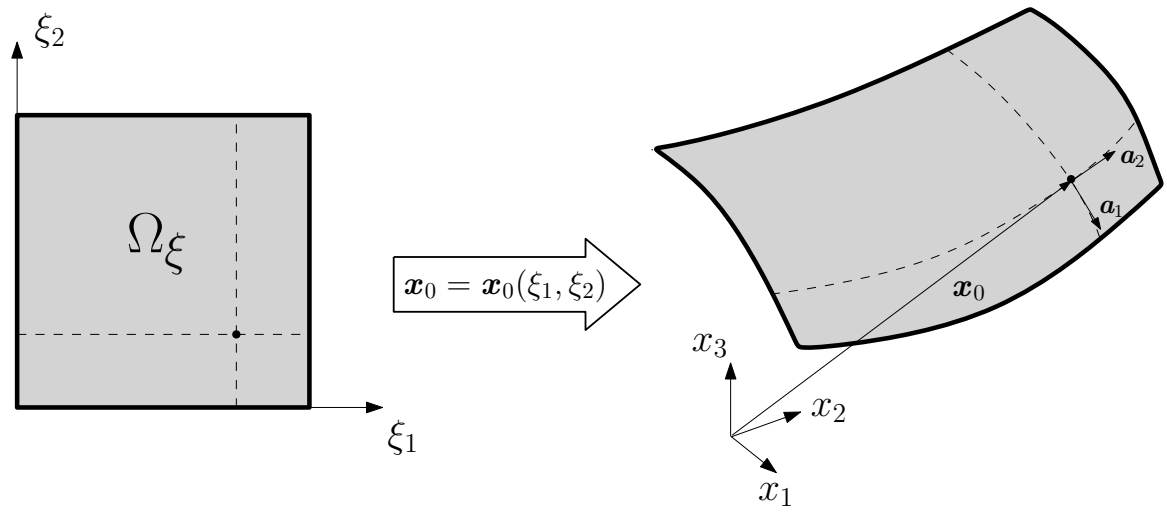

Figure 1: Mapping scheme for the shell mid-surface.

2.2. Shell kinematics

According to the geometrical description introduced in the previous Section, the shell deformation can be described in terms of the displacement vector expressed either in orthogonal components as $\boldsymbol{u} = \{u_1 \; u_2 \; u_3\}^{\mathrm{T}}$ or in covariant components as $\boldsymbol{u}_\xi = \{u_{\xi_1} \; u_{\xi_2} \; u_{\xi_3}\}^{\mathrm{T}}$. The shell kinematics employed to develop the present formulation is based on the expansion of the displacements component across the shell thickness through known functions of ξ_3. Thus, the covariant components u_{ξ_i} of the displacement vector are expressed as

$$u_{\xi_i}(\xi_1, \xi_2, \xi_3) = \sum_{k=0}^{N_i} Z_k^i(\xi_3) U_{ik}(\xi_1, \xi_2) \tag{7}$$

where N_i is the order of the expansion assumed for u_{ξ_i}, $Z_k^i(\xi_3)$ is the k-th function of the expansion of u_{ξ_i} and $U_{ik}(\xi_1, \xi_2)$ are the unknown generalized displacements. It is worth noting that, according to the Carrera Unified Formulation underlying principles [6], in Eq. (7) N_i can be considered as parameters whose values allow to build different order shell structural theories falling within the ESL approach for multilayered structures . The shell

theory corresponding to the expansion orders N_1, N_2 and N_3 is denoted as $\mathrm{ED}_{N_1N_2N_3}$. Collecting the generalized displacements as elements of the vector $\boldsymbol{U}(\xi_1, \xi_2)$, having size $N_U = N_1 + N_2 + N_3 + 3$, and consistently arranging the functions Z_k^i as elements of the matrix $\boldsymbol{Z}(\xi_3)$, the Eq. (7) is compactly rewritten in matrix form as

$$\boldsymbol{u}_\xi = \boldsymbol{Z}(\xi_3)\boldsymbol{U}(\xi_1, \xi_2). \tag{8}$$

and, by using Eqs. (6) and (8), the displacement $\boldsymbol{u}$ in the orthogonal reference system is obtained in terms of the generalized displacement vector $\boldsymbol{U}$ as

$$\boldsymbol{u} = \boldsymbol{R}_\xi \boldsymbol{Z}\boldsymbol{U}. \tag{9}$$

It is observed that the expansion functions $Z_k^i(\xi_3)$ can be chosen without particular restrictions (e.g polynomial, exponential, trigonometric). Here, they are taken as the Taylor polynomials having order $k \leq N_i$ and scaled in the interval I_{ξ_3}. As an example, for the ED_{222} theory, the matrix $\boldsymbol{Z}$ is obtained as

$$\boldsymbol{Z} = \begin{bmatrix} 1 & 2\xi_3/\tau & (2\xi_3/\tau)^2 & 0 & 0 & 0 & 0 & 0 & 0 \\ 0 & 0 & 0 & 1 & 2\xi_3/\tau & (2\xi_3/\tau)^2 & 0 & 0 & 0 \\ 0 & 0 & 0 & 0 & 0 & 0 & 1 & 2\xi_3/\tau & (2\xi_3/\tau)^2 \end{bmatrix} \tag{10}$$

The Green-Lagrange strain components vector, namely $\boldsymbol{\gamma} = \{\gamma_{11}\ \gamma_{22}\ \gamma_{33}\ \gamma_{23}\ \gamma_{13}\ \gamma_{12}\ \}^{\mathrm{T}}$, expressed in the orthogonal reference system is given by

$$\boldsymbol{\gamma} = \left(\boldsymbol{I}_i + \frac{1}{2}\boldsymbol{W}_i\right)\frac{\partial \boldsymbol{u}}{\partial x_i} \tag{11}$$

where the following auxiliary matrices have been introduced

$$\boldsymbol{I}_1 = \begin{bmatrix} 1 & 0 & 0 \\ 0 & 0 & 0 \\ 0 & 0 & 0 \\ 0 & 0 & 0 \\ 0 & 0 & 1 \\ 0 & 1 & 0 \end{bmatrix}, \quad \boldsymbol{I}_2 = \begin{bmatrix} 0 & 0 & 0 \\ 0 & 1 & 0 \\ 0 & 0 & 0 \\ 0 & 0 & 1 \\ 0 & 0 & 0 \\ 1 & 0 & 0 \end{bmatrix}, \quad \boldsymbol{I}_3 = \begin{bmatrix} 0 & 0 & 0 \\ 0 & 0 & 0 \\ 0 & 0 & 1 \\ 0 & 1 & 0 \\ 1 & 0 & 0 \\ 0 & 0 & 0 \end{bmatrix}, \tag{12a}$$

$$\boldsymbol{W}_1 = \begin{bmatrix} \frac{\partial u_1}{\partial x_1} & \frac{\partial u_2}{\partial x_1} & \frac{\partial u_3}{\partial x_1} \\ 0 & 0 & 0 \\ 0 & 0 & 0 \\ 0 & 0 & 0 \\ \frac{\partial u_1}{\partial x_3} & \frac{\partial u_2}{\partial x_3} & \frac{\partial u_3}{\partial x_3} \\ \frac{\partial u_1}{\partial x_2} & \frac{\partial u_2}{\partial x_2} & \frac{\partial u_3}{\partial x_2} \end{bmatrix}, \quad \boldsymbol{W}_2 = \begin{bmatrix} 0 & 0 & 0 \\ \frac{\partial u_1}{\partial x_2} & \frac{\partial u_2}{\partial x_2} & \frac{\partial u_3}{\partial x_2} \\ 0 & 0 & 0 \\ \frac{\partial u_1}{\partial x_3} & \frac{\partial u_2}{\partial x_3} & \frac{\partial u_3}{\partial x_3} \\ 0 & 0 & 0 \\ \frac{\partial u_1}{\partial x_1} & \frac{\partial u_2}{\partial x_1} & \frac{\partial u_3}{\partial x_1} \end{bmatrix}, \quad \boldsymbol{W}_3 = \begin{bmatrix} 0 & 0 & 0 \\ 0 & 0 & 0 \\ \frac{\partial u_1}{\partial x_3} & \frac{\partial u_2}{\partial x_3} & \frac{\partial u_3}{\partial x_3} \\ \frac{\partial u_1}{\partial x_2} & \frac{\partial u_2}{\partial x_2} & \frac{\partial u_3}{\partial x_2} \\ \frac{\partial u_1}{\partial x_1} & \frac{\partial u_2}{\partial x_1} & \frac{\partial u_3}{\partial x_1} \\ 0 & 0 & 0 \end{bmatrix} \tag{12b}$$

The Eq. (11) extends the notation introduced in Ref.[56] including all the nonlinear terms arising in the definition of the strain tensor. It is worth noting that additional assumptions in the definition of the nonlinear strain, e.g. the Von Kármán approximation for plates, can be accounted for by suitably modifying the definition of the matrices $\boldsymbol{W}_i$. Using Eq. (9) and applying the chain rule to express the derivatives in the orthogonal reference system coordinates through those in the curvilinear coordinates, one obtains

$$\frac{\partial \boldsymbol{u}}{\partial x_i} = \boldsymbol{D}_{0i}\boldsymbol{U} + \boldsymbol{D}_{\alpha i}\frac{\partial \boldsymbol{U}}{\partial \xi_\alpha} \tag{13}$$

where

$$\boldsymbol{D}_{0i} = \frac{\partial \xi_j}{\partial x_i}\frac{\partial \boldsymbol{R}_\xi}{\partial \xi_j}\boldsymbol{Z} + \frac{\partial \xi_3}{\partial x_i}\boldsymbol{R}_\xi \frac{\mathrm{d}\boldsymbol{Z}}{\mathrm{d}\xi_3} \tag{14a}$$

$$\boldsymbol{D}_{\alpha i} = \frac{\partial \xi_\alpha}{\partial x_i}\boldsymbol{R}_\xi \boldsymbol{Z} \tag{14b}$$

Finally, upon introducing Eq. (13) in Eqs. (11), the Green-Lagrange strains are expressed as

$$\boldsymbol{\gamma} = \left(\boldsymbol{I}_i + \frac{1}{2}\boldsymbol{W}_i\right)\left(\boldsymbol{D}_{0i}\boldsymbol{U} + \boldsymbol{D}_{\alpha i}\frac{\partial \boldsymbol{U}}{\partial \xi_\alpha}\right) \tag{15}$$

2.3. Constitutive behaviour

Each layer of the laminated shell is assumed to be homogeneous, orthotropic and obeying a generalized Hooke's law, meaning that a linear relationship between the second Piola-Kirchhoff stress tensor and the Green-Lagrange strain tensor holds. As the layers follow the curvature of the shell, the constitutive relationships in the orthogonal reference system depend on the position on the reference domain. At a generic point of the ℓ-th layer, the constitutive law can be expressed in the orthotropic material reference system whose orthonormal basis is given by the vectors

$$\boldsymbol{m}_1^{\langle \ell \rangle} = \boldsymbol{R}_{\boldsymbol{n}_0}(\theta^{\langle \ell \rangle})\frac{\boldsymbol{g}_1}{||\boldsymbol{g}_1||}, \quad \boldsymbol{m}_3^{\langle \ell \rangle} = \boldsymbol{n}_0, \quad \text{and} \quad \boldsymbol{m}_2^{\langle \ell \rangle} = \boldsymbol{m}_3^{\langle \ell \rangle} \times \boldsymbol{m}_1^{\langle \ell \rangle}. \tag{16}$$

where $\boldsymbol{R}_{\boldsymbol{n}_0}(\theta^{\langle \ell \rangle})$ is the transformation matrix that rotate a vector around $\boldsymbol{n}_0$ of an angle correspondent to the lamination angle $\theta^{\langle \ell \rangle}$, which is measured with respect the $\boldsymbol{g}_1$ direction. In this local orthonormal basis, the relationship between the second Piola-Kirchhoff stress $\widetilde{\boldsymbol{\sigma}}^{\langle \ell \rangle} = \{\widetilde{\sigma}_{11}^{\langle \ell \rangle}\ \widetilde{\sigma}_{22}^{\langle \ell \rangle}\ \widetilde{\sigma}_{33}^{\langle \ell \rangle}\ \widetilde{\sigma}_{23}^{\langle \ell \rangle}\ \ \widetilde{\sigma}_{13}^{\langle \ell \rangle}\ \widetilde{\sigma}_{12}^{\langle \ell \rangle}\}^{\mathrm{T}}$ and the Green-Lagrange strains $\widetilde{\boldsymbol{\gamma}}^{\langle \ell \rangle} = \{\widetilde{\gamma}_{11}^{\langle \ell \rangle}\ \widetilde{\gamma}_{22}^{\langle \ell \rangle}\ \widetilde{\gamma}_{33}^{\langle \ell \rangle}\ \widetilde{\gamma}_{23}^{\langle \ell \rangle}\ \ \widetilde{\gamma}_{13}^{\langle \ell \rangle}\ \widetilde{\gamma}_{12}^{\langle \ell \rangle}\}^{\mathrm{T}}$ is given by

$$\widetilde{\boldsymbol{\sigma}}^{\langle \ell \rangle} = \widetilde{\boldsymbol{c}}^{\langle \ell \rangle}\widetilde{\boldsymbol{\gamma}}^{\langle \ell \rangle}. \tag{17}$$

where the stiffness matrix $\widetilde{\boldsymbol{c}}^{\langle\ell\rangle}$ is obtained from the orthotropic material properties as given in Appendix A. The constitutive matrix $\boldsymbol{c}^{\langle\ell\rangle}$ expressed in the orthogonal reference system $x_1x_2x_3$ is then deduced applying the 4-th rank tensor transformation of axes formulas to $\widetilde{\boldsymbol{c}}^{\langle\ell\rangle}$ obtaining

$$\boldsymbol{\sigma}^{\langle\ell\rangle} = \boldsymbol{T}\ \widetilde{\boldsymbol{c}}^{\langle\ell\rangle}\boldsymbol{T}^{\mathrm{T}}\boldsymbol{\gamma} = \boldsymbol{c}^{\langle\ell\rangle}\boldsymbol{\gamma} \tag{18}$$

where $\boldsymbol{\sigma}^{\langle\ell\rangle} = \{\sigma_{11}^{\langle\ell\rangle}\ \sigma_{22}^{\langle\ell\rangle}\ \sigma_{33}^{\langle\ell\rangle}\ \sigma_{23}^{\langle\ell\rangle}\ \ \sigma_{13}^{\langle\ell\rangle}\ \sigma_{12}^{\langle\ell\rangle}\}^{\mathrm{T}}$ is the vector of the stress components in the orthogonal reference system and the transformation matrix $\boldsymbol{T}$ is defined in Appendix A.

2.4. Principle of virtual works

The governing equations for the introduced shell models are inferred from the principle of virtual works that reads as

$$\delta L_{int} = \delta L_{ext} \tag{19}$$

where δL_{int} and δL_{ext} are the virtual work of the internal and external forces, respectively. For a multilayered structure they are expressed as

$$\delta L_{int} = \sum_{\ell=1}^{N_\ell} \int_{V^{\langle\ell\rangle}} \delta\boldsymbol{\gamma}^{\mathrm{T}}\boldsymbol{\sigma}^{\langle\ell\rangle}\mathrm{d}V \tag{20a}$$

$$\delta L_{ext} = \sum_{\ell=1}^{N_\ell} \int_{V^{\langle\ell\rangle}} \delta\boldsymbol{u}^{\mathrm{T}}\overline{\boldsymbol{b}}\mathrm{d}V + \sum_{\ell=1}^{N_\ell} \int_{\partial V^{\langle\ell\rangle}} \delta\boldsymbol{u}^{\mathrm{T}}\overline{\boldsymbol{t}}\mathrm{d}\partial V, \tag{20b}$$

where $\overline{\boldsymbol{b}}$ and $\overline{\boldsymbol{t}}$ are the volume forces acting on $V^{\langle\ell\rangle}$ and the applied tractions acting on $\partial V^{\langle\ell\rangle}$, respectively. From Eq. (11) the virtual strains are given by

$$\delta\boldsymbol{\gamma} = (\boldsymbol{I}_i + \boldsymbol{W}_i)\frac{\partial\delta\boldsymbol{u}}{\partial x_i} \tag{21}$$

Inserting Eqs (21), (18) and (11) into Eq.(20a), the virtual internal work is written as

$$\delta L_{int} = \sum_{\ell=1}^{N_\ell} \int_{V^{\langle \ell \rangle}} \frac{\partial \delta \boldsymbol{u}}{\partial x_i}^{\mathrm{T}} \boldsymbol{C}_{ij} \frac{\partial \boldsymbol{u}}{\partial x_j}, \tag{22}$$

where

$$\boldsymbol{C}_{ij} = \left(\boldsymbol{I}_i^{\mathrm{T}} + \boldsymbol{W}_i^{\mathrm{T}}\right) \boldsymbol{c}^{\langle \ell \rangle} \left(\boldsymbol{I}_i + \frac{1}{2}\boldsymbol{W}_i\right). \tag{23}$$

Furthermore, introducing Eq. (13) into Eq.(22) and integrating along the thickness, one obtains

$$\delta L_{int} = \int_{\Omega_\xi} \left[\frac{\partial \delta \boldsymbol{U}^{\mathrm{T}}}{\partial \xi_\alpha} \left(\boldsymbol{Q}_{\alpha\beta} \frac{\partial \boldsymbol{U}}{\partial \xi_\beta} + \boldsymbol{R}_{\alpha 3} \boldsymbol{U} \right) + \delta \boldsymbol{U}^{\mathrm{T}} \left(\boldsymbol{R}_{3\alpha} \frac{\partial \boldsymbol{U}}{\partial \xi_\alpha} + \boldsymbol{S}_{33} \boldsymbol{U} \right) \right] \mathrm{d}\Omega_\xi, \tag{24}$$

where the generalized stiffness matrices are introduced as

$$\boldsymbol{Q}_{\alpha\beta} = \sum_{\ell=1}^{N_\ell} \int_{\xi_{3b}^{\langle \ell \rangle}}^{\xi_{3t}^{\langle \ell \rangle}} \boldsymbol{D}_{\alpha i}^{\mathrm{T}} \boldsymbol{C}_{ij} \boldsymbol{D}_{\beta j} \sqrt{g} \, \mathrm{d}\xi_3 \tag{25a}$$

$$\boldsymbol{R}_{\alpha 3} = \sum_{\ell=1}^{N_\ell} \int_{\xi_{3b}^{\langle \ell \rangle}}^{\xi_{3t}^{\langle \ell \rangle}} \boldsymbol{D}_{\alpha i}^{\mathrm{T}} \boldsymbol{C}_{ij} \boldsymbol{D}_{0 j} \sqrt{g} \, \mathrm{d}\xi_3 \tag{25b}$$

$$\boldsymbol{R}_{3\alpha} = \sum_{\ell=1}^{N_\ell} \int_{\xi_{3b}^{\langle \ell \rangle}}^{\xi_{3t}^{\langle \ell \rangle}} \boldsymbol{D}_{0 i}^{\mathrm{T}} \boldsymbol{C}_{ij} \boldsymbol{D}_{\alpha j} \sqrt{g} \, \mathrm{d}\xi_3 \tag{25c}$$

$$\boldsymbol{S}_{33} = \sum_{\ell=1}^{N_\ell} \int_{\xi_{3b}^{\langle \ell \rangle}}^{\xi_{3t}^{\langle \ell \rangle}} \boldsymbol{D}_{0 i}^{\mathrm{T}} \boldsymbol{C}_{ij} \boldsymbol{D}_{0 j} \sqrt{g} \, \mathrm{d}\xi_3, \tag{25d}$$

being g the determinant of the metric tensor. Similarly, introducing Eq. (9) into Eq. (20b) and integrating along the thickness, for the external forces virtual work one writes

$$\delta L_{ext} = \int_{\Omega_\xi} \delta \boldsymbol{U}^{\mathrm{T}} \overline{\boldsymbol{B}} \, \mathrm{d}\Omega_\xi + \int_{\partial\Omega_\xi} \delta \boldsymbol{U}^{\mathrm{T}} \overline{\boldsymbol{T}} \, \mathrm{d}\partial\Omega_\xi, \tag{26}$$

where $\overline{\boldsymbol{B}}$ and $\overline{\boldsymbol{T}}$ are the generalized domain forces and the generalized boundary forces, respectively. They are defined, as

$$\overline{\boldsymbol{B}} = \boldsymbol{Z}^{\mathrm{T}} \boldsymbol{R}_{\xi}^{\mathrm{T}} \overline{\boldsymbol{t}} \sqrt{g} \sqrt{n_i g^{ij} n_j} \, \Big|_{\xi_3 = \pm \tau/2} + \sum_{\ell=1}^{N_\ell} \int_{\xi_{3b}^{\langle \ell \rangle}}^{\xi_{3t}^{\langle \ell \rangle}} \boldsymbol{Z}^{\mathrm{T}} \boldsymbol{R}_{\xi}^{\mathrm{T}} \overline{\boldsymbol{b}} \sqrt{g} \, \mathrm{d}\xi_3, \tag{27a}$$

$$\overline{\boldsymbol{T}} = \sum_{\ell=1}^{N_\ell} \int_{\xi_{3b}^{\langle \ell \rangle}}^{\xi_{3t}^{\langle \ell \rangle}} \boldsymbol{Z}^{\mathrm{T}} \boldsymbol{R}_{\xi}^{\mathrm{T}} \overline{\boldsymbol{t}} \sqrt{g} \sqrt{n_i g^{ij} n_j} \, \mathrm{d}\xi_3. \tag{27b}$$

where the notation $f|_{\xi_3 = \bar{\xi}_3}$ indicates evaluation of f at $\xi_3 = \overline{\xi}_3$

Finally, the following expression of the principle of virtual works for the non-linear static analysis of multilayered shells is obtained, which represents the weak form of the problem governing equations

$$\begin{aligned} \int_{\Omega_\xi} \left[\frac{\partial \delta \boldsymbol{U}^{\mathrm{T}}}{\partial \xi_\alpha} \left(\boldsymbol{Q}_{\alpha\beta} \frac{\partial \boldsymbol{U}}{\partial \xi_\beta} + \boldsymbol{R}_{\alpha 3} \boldsymbol{U} \right) + \delta \boldsymbol{U}^{\mathrm{T}} \left(\boldsymbol{R}_{3\alpha} \frac{\partial \boldsymbol{U}}{\partial \xi_\alpha} + \boldsymbol{S}_{33} \boldsymbol{U} \right) \right] \mathrm{d}\Omega_\xi = \\ \int_{\Omega_\xi} \delta \boldsymbol{U}^{\mathrm{T}} \overline{\boldsymbol{B}} \, \mathrm{d}\Omega_\xi + \int_{\partial\Omega_\xi} \delta \boldsymbol{U}^{\mathrm{T}} \overline{\boldsymbol{T}} \, \mathrm{d}\partial\Omega_\xi \end{aligned} \tag{28}$$

After integration by parts of the Eq. (28), ensuring that the resulting relation holds for any virtual variation of the primary variables provides the following shell governing equations and the associated natural boundary conditions

$$-\frac{\partial}{\partial \xi_\alpha} \left(\boldsymbol{Q}_{\alpha\beta} \frac{\partial \boldsymbol{U}}{\partial \xi_\beta} + \boldsymbol{R}_{\alpha 3} \boldsymbol{U} \right) + \boldsymbol{R}_{3\alpha} \frac{\partial \boldsymbol{U}}{\partial \xi_\alpha} + \boldsymbol{S}_{33} \boldsymbol{U} = \overline{\boldsymbol{B}} \qquad \text{in } \Omega_\xi \tag{29a}$$

$$\nu_\alpha \left(\boldsymbol{Q}_{\alpha\beta} \frac{\partial \boldsymbol{U}}{\partial \xi_\beta} + \boldsymbol{R}_{\alpha 3} \boldsymbol{U} \right) = \overline{\boldsymbol{T}} \qquad \text{on } \partial\Omega_{\xi N} \tag{29b}$$

where ν_α are the direction cosines of the outer unit normal defined over the part $\partial\Omega_{\xi N}$ of the Ω_ξ domain where natural boundary conditions are prescribed.

3. Discontinuous Galerkin formulation

The solution of the problem governing equations, stated in weak form by Eq. (28), is addressed through the Pure Penalty discontinuous Galerkin (dG) method introduced by Babuška in [63] for the Poisson problem and in [64] for the Kirchhoff plate problem with homogeneous boundary conditions, and also employed by Gulizzi et al. in [56, 57] for linear analysis of multilayered plates.

3.1. Pure Penalty discontinuous Galerkin method

Following the standard procedure for dG methods, the shell reference domain Ω_ξ is partitioned into N_e elements. For the sake of simplicity and without lack of generality, a simple rectangular mesh is adopted in this work; therefore, the domain of the e-th element Ω_ξ^e is identified by $\Omega_\xi^e \equiv [\xi_{1b}^e, \xi_{1t}^e] \times [\xi_{2b}^e, \xi_{2t}^e]$, where ξ_{ib}^e and ξ_{it}^e are the minimum and maximum values for ξ_i within the e-th element. Note that the superscript e is used to denote quantities referred to the e-th element.

The primal form of the Pure Penalty dG method adopted in this work is stated as

$$B(\boldsymbol{V}, \boldsymbol{U}_h) = F(\boldsymbol{V}, \overline{\boldsymbol{B}}, \overline{\boldsymbol{T}}, \overline{\boldsymbol{U}}), \quad \forall \boldsymbol{V} \in \boldsymbol{\mathcal{V}}_{hp}^U. \tag{30}$$

where

$$B(\boldsymbol{V}, \boldsymbol{U}_h) = \int_{\Omega_\xi^h} \left[\frac{\partial \boldsymbol{V}^{\mathrm{T}}}{\partial \xi_\alpha} \left(\boldsymbol{Q}_{\alpha\beta} \frac{\partial \boldsymbol{U}_h}{\partial \xi_\beta} + \boldsymbol{R}_{\alpha 3} \boldsymbol{U}_h \right) + \boldsymbol{V}^{\mathrm{T}} \left(\boldsymbol{R}_{3\alpha} \frac{\partial \boldsymbol{U}_h}{\partial \xi_\alpha} + \boldsymbol{S}_{33} \boldsymbol{U}_h \right) \right] + \int_{\partial\Omega_{\xi I}^h} \mu [\![\boldsymbol{V}]\!]_\alpha^{\mathrm{T}} [\![\boldsymbol{U}_h]\!]_\alpha + \int_{\partial\Omega_{\xi D}^h} \mu \boldsymbol{V}^{\mathrm{T}} \boldsymbol{U}_h \tag{31a}$$

$$F(\boldsymbol{V}, \overline{\boldsymbol{B}}, \overline{\boldsymbol{T}}, \overline{\boldsymbol{U}}) \equiv \int_{\Omega_\xi^h} \boldsymbol{V}^{\mathrm{T}} \overline{\boldsymbol{B}} + \int_{\partial\Omega_{\xi N}^h} \boldsymbol{V}^{\mathrm{T}} \overline{\boldsymbol{T}} + \int_{\partial\Omega_{\xi D}^h} \mu \boldsymbol{V}^{\mathrm{T}} \overline{\boldsymbol{U}}, \tag{31b}$$

being $\boldsymbol{U}_h$ the approximation of the generalized displacements field resulting from the solution of the dG statement, $\boldsymbol{V}$ the test functions belonging to the space $\boldsymbol{\mathcal{V}}_{hp}^{U}$ and $\overline{\boldsymbol{U}}$ the prescribed values of the generalized displacements stemming from the essential boundary conditions of the problem. The integrals appearing in Eqs.(31) are typically referred to as broken integrals and their definitions are

$$\int_{\Omega_\xi^h} \bullet \equiv \sum_{e=1}^{N_e} \int_{\Omega_\xi^e} \bullet^e \, \mathrm{d}\Omega_\xi \tag{32a}$$

$$\int_{\partial\Omega_{\xi I}^h} \bullet \equiv \sum_{i=1}^{N_i} \int_{\partial\Omega_{\xi I}^i} \bullet^i \, \mathrm{d}\partial\Omega_\xi \tag{32b}$$

$$\int_{\partial\Omega_{\xi D}^h} \bullet \equiv \sum_{e=1}^{N_e} \int_{\partial\Omega_{\xi D}^e} \bullet^e \, \mathrm{d}\partial\Omega_\xi \tag{32c}$$

$$\int_{\partial\Omega_{\xi N}^h} \bullet \equiv \sum_{e=1}^{N_e} \int_{\partial\Omega_{\xi N}^e} \bullet^e \, \mathrm{d}\partial\Omega_\xi \tag{32d}$$

where Ω_ξ^h is the approximation of Ω_ξ that is obtained collecting the domains Ω_ξ^e of the elements, $\partial\Omega_{\xi I}^h$ is the collection of the N_i inter-element interfaces $\partial\Omega_{\xi I}^i$ that are generated partitioning the reference domain, $\partial\Omega_{\xi D}^h$ and $\partial\Omega_{\xi N}^h$ are the collections of the elements portions of boundaries $\partial\Omega_\xi^e$ and $\partial\Omega_{\xi N}^e$ where the essential and natural boundary conditions are enforced, respectively. Moreover, in Eqs. (32) the *jump* operator $[\![\bullet]\!]_\alpha^{(i)} \equiv \nu_\alpha^e \, \bullet^e + \nu_\alpha^{e'} \bullet^{e'}$ appears, being $\boldsymbol{\nu}^e = \{\nu_1^e \ \nu_2^e\}^{\mathrm{T}}$ and $\boldsymbol{\nu}^{e'} = \{\nu_1^{e'} \ \nu_2^{e'}\}^{\mathrm{T}}$ the outer unit normal vectors defined over $\partial\Omega_\xi^e$ and $\partial\Omega_\xi^{e'}$, respectively.

In the primal form of the Pure Penalty dG method, namely Eqs. (30) and (31), μ is the penalty parameter used to enforce the inter-elements continuity of the solution and the essential boundary conditions through the corresponding integrals over $\partial\Omega_{\xi I}^h$ and $\partial\Omega_{\xi D}^h$, respectively. The choice of μ is crucial for the method to be efficient: a too small penalty

value leads high discontinuities of the solution across the interfaces of the elements and a too high penalty causes an ill-conditioning of the resolving system. A typical choice of the penalty parameter in the Pure Penalty dG formulation is $\mu = Q/h^{2p}$ where Q is a sufficiently large constant, typically proportional to the highest Young modulus of the structure materials, and h is a characteristic mesh size [34]. It is remarked that differently from other dG formulation, such as the Interior Penalty [65], in the Pure Penalty one the value of μ has to be significantly higher and this has an adverse effect on the condition number of the resolving system matrix [66]. On the other hand, the primal form associated with the Pure Penalty approach accounts for integrals over the elements boundaries not involving the internal forces, which are nonlinear for the problem in hand [56]. Actually these boundary integrals are linear with respect to $\boldsymbol{U}_h$ and therefore they do not need to be computed for each iteration of the solution scheme with consequent computational advantages. For more details on the dG formulation development the reader is referred to [56].

3.2. Non-linear resolving system

The statement in Eq. (30) is transformed into an algebraic system by choosing an adequate approximation expansions for the test functions $\boldsymbol{V}$ and the primary variables $\boldsymbol{U}_h$. These are chosen within a space of discontinuous polynomial basis functions as detailed in [34, 56, 57]. In particular, the k-th components V_k^e and U_k^e of the restriction $\boldsymbol{V}^e$ and $\boldsymbol{U}_h^e$ of the fields $\boldsymbol{V}$ and $\boldsymbol{U}_h$ to the e-th element are approximated as

$$U_k^e = \sum_{p_1=0}^{p} \sum_{p_2=0}^{p} \boldsymbol{\mathcal{L}}_{p_1}^e(\xi_1) \boldsymbol{\mathcal{L}}_{p_2}^e(\xi_2) X_{p_1 p_2}^{ek} \tag{33a}$$

$$V_k^e = \sum_{p_1=0}^{p} \sum_{p_2=0}^{p} \boldsymbol{\mathcal{L}}_{p_1}^e(\xi_1) \boldsymbol{\mathcal{L}}_{p_2}^e(\xi_2) \delta X_{p_1 p_2}^{ek} \tag{33b}$$

where $\mathcal{L}^e_{p_j}(\xi_j)$ is the Legendre polynomial of order p_j scaled in the interval $[\xi^e_{jb}, \xi^e_{jt}]$, $X^{ek}_{p_1p_2}$ are the unknown expansion coefficients and $\delta X^{ek}_{p_1p_2}$ are the arbitrary parameters of the test function. Accordingly, in compact matrix form, one writes

$$\boldsymbol{U}^e_h = \boldsymbol{P}^e(\xi_1, \xi_2)\boldsymbol{X}^e, \tag{34a}$$

$$\boldsymbol{V}^e = \boldsymbol{P}^e(\xi_1, \xi_2)\delta\boldsymbol{X}^e \tag{34b}$$

where the vectors $\boldsymbol{X}^e$ and $\delta\boldsymbol{X}^e$ collect the unknowns $X^{ek}_{p_1p_2}$ and the parameters of the test function $\delta X^{ek}_{p_1p_2}$, respectively, while the matrix $\boldsymbol{P}^e(\xi_1, \xi_2)$ consistently collects the functions used for the expansion of the components of $\boldsymbol{U}^e_h$ and $\boldsymbol{V}^e$.

Substituting the expressions of $\boldsymbol{U}^e_h$ and $\boldsymbol{V}^e$ into Eq. (30) one obtains the Pure Penalty dG discrete primal form and applying the standard variational calculus procedure the following nonlinear algebraic system is inferred

$$\boldsymbol{K}(\boldsymbol{X})\boldsymbol{X} = \boldsymbol{F}, \tag{35}$$

where the vector $\boldsymbol{X}$ collect as blocks the vectors $\boldsymbol{X}^e$ in such way that the degrees of freedom corresponding to the same element appear as a sequence within $\boldsymbol{X}$. The stiffness matrix $\boldsymbol{K}$ can be decomposed into three kinds of contributes, namely $\boldsymbol{K} = \boldsymbol{K}_I + \boldsymbol{K}_{II} + \boldsymbol{K}_{III}$, which originates from the work of internal forces, the enforcement of the continuity of the solution across the elements and the enforcement of the problem essential boundary conditions, respectively. Thus, the stiffness matrix $\boldsymbol{K}$ and the right-hand-side $\boldsymbol{F}$ are consistently obtained by an assembly procedure resting on the following rules:

a. the e-th element provides

– the contribution to the stiffness matrix $\boldsymbol{K}$ stemming from the work of the internal

forces given by

$$\boldsymbol{K}_I^e = \int_{\Omega_\xi^e} \left[\frac{\partial \boldsymbol{P}^{e\mathrm{T}}}{\partial \xi_\alpha} \left(\boldsymbol{Q}_{\alpha\beta} \frac{\partial \boldsymbol{P}^e}{\partial \xi_\beta} + \boldsymbol{R}_{\alpha 3} \boldsymbol{P}^e \right) + \boldsymbol{P}^{e\mathrm{T}} \left(\boldsymbol{R}_{3\alpha} \frac{\partial \boldsymbol{P}^e}{\partial \xi_\alpha} + \boldsymbol{S}_{33} \boldsymbol{P}^e \right) \right] \mathrm{d}\Omega_\xi, \quad (36)$$

and that sums to the rows and columns associated with the degrees of freedom of the element;

– the contribution to the right-hand-side $\boldsymbol{F}$ due to the body forces, given by

$$\boldsymbol{F}_b^e = \int_{\Omega_\xi^e} \boldsymbol{P}^{e\mathrm{T}} \overline{\boldsymbol{B}} \, \mathrm{d}\Omega_\xi \quad (37)$$

and that sums to the rows associated with the degrees of freedom of the element;

– the contribution to the right-hand-side $\boldsymbol{F}$ due to the boundary forces, given by

$$\boldsymbol{F}_t^e = \int_{\partial\Omega_{\xi N}^e} \boldsymbol{P}^{e\mathrm{T}} \overline{\boldsymbol{T}} \, \mathrm{d}\partial\Omega_\xi \quad (38)$$

and that sums to the rows associated with the degrees of freedom of the element;

– the contributions due to the essential boundary conditions that are given by

$$\boldsymbol{K}_{III}^e = \int_{\partial\Omega_{\xi D}^e} \mu \boldsymbol{P}^{e\mathrm{T}} \boldsymbol{P}^e \, \mathrm{d}\partial\Omega_\xi \quad (39)$$

that sums to the $\boldsymbol{K}$ matrix at the rows and columns associated with the degrees of freedom of the element, and

$$\boldsymbol{F}_u^e = \int_{\partial\Omega_{\xi D}^e} \mu \boldsymbol{P}^{e\mathrm{T}} \overline{\boldsymbol{U}} \, \mathrm{d}\partial\Omega_\xi \quad (40)$$

that sums to the right-hand-side $\boldsymbol{F}$ at the row associated with the degrees of freedom of the element.

b. the i-th interface between the elements e and e' provides four contributions to the stiffness matrix $\boldsymbol{K}$ enforcing the inter-element continuity, namely

– the contribution

$$\boldsymbol{K}_{II}^{iee} = \int_{\partial\Omega_{\xi I}^{i}} \mu \boldsymbol{P}^{e\mathrm{T}} \boldsymbol{P}^{e} \, \mathrm{d}\partial\Omega_{\xi}, \tag{41}$$

that sums to the rows and columns associated with the degrees of freedom of the e-th element;

– the contribution

$$\boldsymbol{K}_{II}^{iee'} = \int_{\partial\Omega_{\xi I}^{i}} \mu \boldsymbol{P}^{e\mathrm{T}} \boldsymbol{P}^{e'} \, \mathrm{d}\partial\Omega_{\xi} \tag{42}$$

that sums to the rows associated with the degrees of freedom of the e-th and the columns associated with the degrees of freedom of the e'-th elements;

– the contribution

$$\boldsymbol{K}_{II}^{ie'e} = \int_{\partial\Omega_{\xi I}^{i}} \mu \boldsymbol{P}^{e'\mathrm{T}} \boldsymbol{P}^{e} \, \mathrm{d}\partial\Omega_{\xi} \tag{43}$$

that sums to the rows associated with the degrees of freedom of the e'-th and the columns associated with the degrees of freedom of the e-th elements;

– the contribution

$$\boldsymbol{K}_{II}^{ie'e'} = \int_{\partial\Omega_{\xi I}^{i}} \mu \boldsymbol{P}^{e'\mathrm{T}} \boldsymbol{P}^{e'} \mathrm{d}\partial\Omega_{\xi} \tag{44}$$

that sums to the rows and columns associated with the degrees of freedom of the e'-th element;

The non-linear algebraic system in Eq. (35) is solved using a Newton-Raphson method with the path-following arc-length iteration scheme proposed by Crisfield [67, 68]. To apply this solution procedure the tangent stiffness matrix $\boldsymbol{K}_T$ is required and then its expression has been derived as reported in Appendix B.

4. Results

To validate the proposed method and assess its capabilities, numerical tests are performed considering different plates and shells benchmark problems. The material properties employed in the analyses are given in Table 1. The presented results refer to three different theories, namely the ED_{kkk} with $k = 1, 2, 3$. For the ED_{kkk} theory, each covariant component of the displacement vector is expanded using Taylor's polynomials up to the k–th order; for the ED_{111}, the material stiffness matrix is also modified according to the plane stress state hypothesis and to keep a shear stress factor equal to 5/6. In all the proposed examples, the penalty parameter has been suitably chosen according to the findings reported in Refs. [56, 34]. Four tests are presented: the nonlinear bending of an isotropic plate, the post-buckling analysis of an isotropic slender plate, the snap-back and snap-through of isotropic and laminated cylindrical shells and the nonlinear response of a complex geometry composite shell. The first three of these tests are popular benchmarks and they allow the present results to be compared with solutions available in the literature. The last case is presented to illustrate the method capabilities in dealing with complex, general shell geometries and its solution is compared with finite elements results.

Table 1: Material properties.

Material ID	**Property**	**Component**	**Value**
M_1	Young's modulus	E	75000 MPa
	Poisson's ratios	ν	0.3
M_2	Young's modulus	E	75000 MPa
	Poisson's ratios	ν	0.316
M_3	Young's modulus	E	3102.75 MPa
	Poisson's ratios	ν	0.3
M_4	Young's moduli	E_1	3300 MPa
		E_2, E_3	1100 MPa
	Poisson's ratios	ν_{23}, ν_{13}, ν_{12}	0.25
	Shear moduli	G_{23}	660 MPa
		G_{13}, G_{12}	660 MPa

4.1. Isotropic plate nonlinear bending

The first validation test regards the nonlinear bending of a constant thickness, isotropic, square plate referred to the $x_1x_2x_3$ orthogonal coordinate system with origin in the mid-plane at a plate corner, the x_1 and x_2 axes directed along the edges and the x_3 axis directed along the plate thickness. The plate is subjected to a uniform surface load q applied on its upper surface and constantly oriented along the x_3 axis during the deformation. The map of the mid surface of the plate is obtained as $x_{01} = \xi_1$, $x_{02} = \xi_2$ and $x_{03} = 0$, where $\xi_1, \xi_2 \in [0, L]$, being $L = 1200$ mm the plate edge length. The plate consists of a single layer with material properties as M1 in Table 1 and thickness τ. Two different values for the thickness have been investigated corresponding to a thin plate having thickness ratio $\tau/L = 0.02$ and a moderately thick plate with $\tau/L = 0.1$. Two sets of boundary conditions

are considered: *i*) all edges clamped, labeled as CCCC, corresponding to $u_{\xi_1} = u_{\xi_2} = u_{\xi_3} = 0$ at the edge points of coordinates $(0, \xi_2, \xi_3)$, (ξ_1, L, ξ_3), (L, ξ_2, ξ_3) and $(\xi_1, 0, \xi_3)$; *ii*) all edges simply-supported, labeled as SSSS, where $u_{\xi_1} = u_{\xi_2} = u_{\xi_3} = 0$ at the edge points of coordinates $(0, \xi_2, 0)$, $(\xi_1, L, 0)$, $(L, \xi_2, 0)$ and $(\xi_1, 0, 0)$.

To assess the efficiency of the method, the *hp*-convergence for different theories was investigated. The reference solution $\boldsymbol{U}_{ref}$ employed for the convergence studies has been obtained by the present method with a 4×4 grid of elements with polynomial trial function of order $p = 7$, which can be considered as converged. For the simply-supported panel with $\tau/L = 0.1$ and the ED_{111} and ED_{333} theories, Fig. 2(a) and 2(b) show the solution error versus the element size measure $h = 1/\sqrt{N_e}$ for different approximation polynomial order p; the error is computed at the step corresponding to a non-dimensional surface load $\overline{q} = qL^4/(E\tau^4) = 400$ as

$$e(\boldsymbol{U}_h) = \frac{|\boldsymbol{U}_h - \boldsymbol{U}_{ref}|_\infty}{|\boldsymbol{U}_h|_\infty} \tag{45}$$

where $|\cdot|_\infty$ is the ∞-norm defined over Ω_ξ. It is worth to note that the number of degrees of freedom associated with the theory $\text{ED}_{k_1k_2k_3}$ is equal to $(k_1 + k_2 + k_3 + 3)(p+1)^2 N_e$. The data of Figs. 2(a-b) evidences that higher polynomial orders are characterized by higher convergence rates and lower errors. These findings are confirmed by similar studies carried out for different cases whose results are not reported here for the sake of brevity. To complement the illustration of the method convergence characteristics, Fig. 2(c-d) show the plate equilibrium paths in terms of the non-dimensional surface load $\overline{q} = p_0 L^4/E\tau^4$ and the transverse displacement at the central point of the plate $\overline{u}_3 = u_3/\tau$. They refer to the case of $\tau/L = 0.1$ and simply-supported edges, analysed by the ED_{111} theory. In particular, Fig. 2(c) shows solutions for different polynomials orders and fixed spatial discretization, whereas Fig. 2(d) reports the solutions for fixed approximating polynomials

order and different number of elements N_e arranged in an $m \times m$ regular grid.

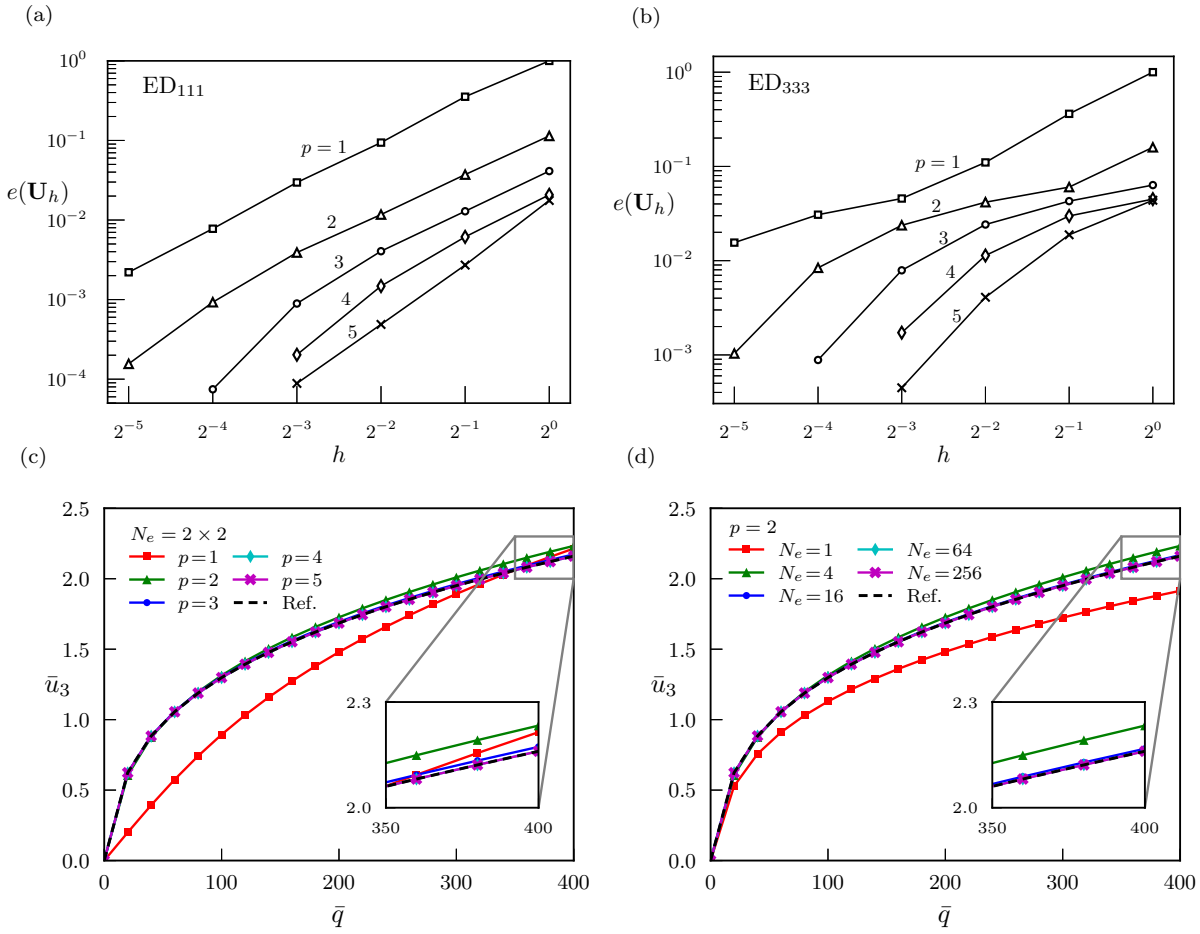

Figure 2: Convergence study for the simply-supported, isotropic, square plate with edge length $L = 1200$ mm and thickness ratio $\tau/L = 0.1$. Convergence is assessed with respect a reference solution (labeled as Ref. in the figures), which is obtained by the present method using a 4×4 grid with elements polynomial trial function order $p = 7$. (a) and (b) show the curves of the solution error $e(\boldsymbol{U}_h)$ versus the element size h for the ED_{111} and the ED_{333} theories, respectively. Curves correspond to different approximation polynomial order p. (c) and (d) show the convergence of the ED_{111} equilibrium path of the non-dimensional transverse displacement $\overline{u}_3 = u_3/\tau$ at the plate central point for different polynomial orders p and constant number of elements N_e and for different number of elements N_e and fixed approximation polynomial order p, respectively.

For the considered boundary conditions and thickness ratios, Fig.(3) shows the plate equilibrium paths in terms of the non-dimensional surface load $\overline{q} = p_0 L^4/E\tau^4$ and transverse displacement at the central point of the plate $\overline{u}_3 = u_3/\tau$. The presented results

are computed through a 2×2 mesh grid of quadrilateral elements with polynomial trial functions of order $p = 5$ and they refer to the solution of the ED_{111} and ED_{333} models, which consists of 864 and 1728 degrees of freedom, respectively. The results are compared with those reported in Ref.[69], in which the FSDT with Von Karman geometrical nonlinearities is employed, and in Ref.[10] whose solution is based on a second order theory. It is noticed that in general there is good agreement between the present and reference results. In particular, for thick plates there is an excellent agreement for the high-order theory whereas contained differences are observed for the FSDT case (Fig. 3(b)). As regard the case of thin plates (Fig. 3(a)) excellent agreement is remarked for the simply-supported boundary conditions whereas for the clamped plate the dG solution appears less stiff.

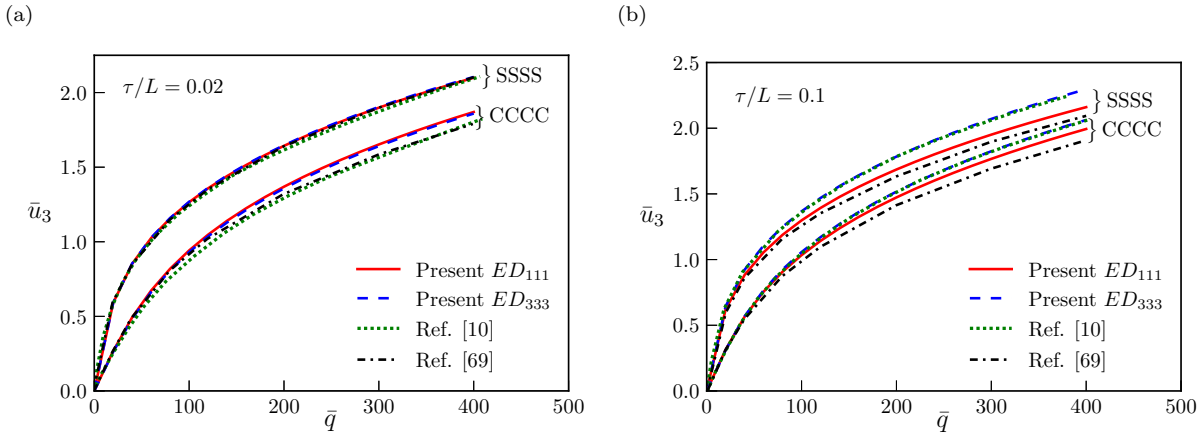

Figure 3: Nonlinear bending equilibrium paths of the isotropic square plates with edge length $L = 1200$ mm, different thickness ratio τ/L and different boundary conditions, namely simply-supported (SSSS) and clamped (CCCC) edges. The curves show the non-dimensional transverse displacement at the central point of the plate $\overline{u}_3 = u_3/\tau$ versus the non-dimensional surface load $\overline{q} = p_0 L^4/E\tau^4$. Present results for the ED_{111} and ED_{333} models, computed through a 2×2 mesh grid of quadrilateral elements with polynomial trial functions of order $p = 5$, and literature solutions are plotted. (a) Thin plate case with $\tau/L = 0.02$. (b) Thick plate case with $\tau/L = 0.1$.

4.2. Post-buckling of isotropic plate

The second test regards the post-buckling behaviour of an isotropic, slender, rectangular plate with edge lengths $a = 300$ mm and $b = 60$ mm and thickness ratio $\tau/b = 0.1$, see Fig. 4(a).

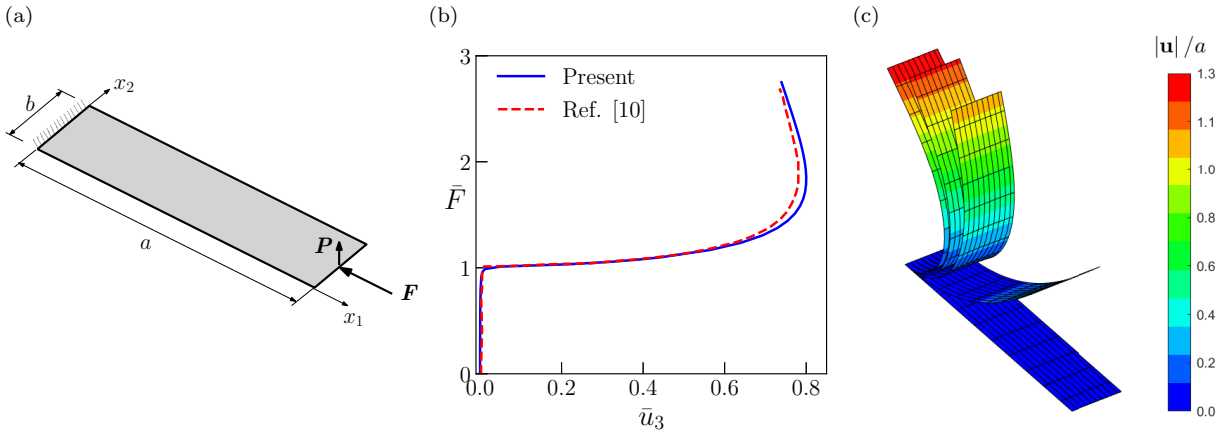

Figure 4: Post-buckling response of the cantilevered, isotropic, slender, rectangular plate with edge lengths $a = 300$ mm and $b = 60$ mm and thickness ratio $\tau/b = 0.1$ under the compression load $\boldsymbol{F}$ and the perturbation load $\boldsymbol{P}$. (a) Plate geometry, loads and boundary conditions. (b) Equilibrium path in terms of non-dimensional transverse displacement $\overline{u}_3 = u_3/a$ at the compression load application point versus the non-dimensional load amplitude $\overline{F} = F(48a^2)/(\pi^2 E b \tau^3)$. Results refer to the ED_{222} theory solved by a 2×2 mesh grid of elements with polynomial trial function order $p = 5$. (c) Post-buckling configurations of the plate for different equilibrium states corresponding to the following compression loads $\overline{F} = 0.0, 1.1, 1.72, 2.27, 2.75$. The color map represents the normalized displacement magnitude $|\boldsymbol{u}|/a$.

The material properties employed correspond to those of material M2 in Table 1. The reference system $x_1x_2x_3$ and the map of the plate are the same as in the previous case with $\xi_1 \in [0, a]$ and $\xi_2 \in [0, b]$. The plate is clamped on one edge, meaning $u_{\xi_1} = u_{\xi_2} = u_{\xi_3} = 0$ at $\xi_1 = 0$, while the other edges are free. A compression point load $\boldsymbol{F}$ is applied at the coordinates $(\xi_1 = a, \xi_2 = b/2, \xi_3 = 0)$, being constantly directed along the direction of x_1. Additionally, in order to enforce post-buckling behaviour, a perturbation consisting of a small concentrated load $\boldsymbol{P}$ directed along x_3 is applied at the point of coordinates

$\xi_1 = a, \xi_2 = b/2, \xi_3 = \tau/2$. The results presented in the following have been obtained through the ED_{222} theory solved by a 2×2 mesh grid of elements with polynomial trial function order $p = 5$, which provides a resolving system with 1296 degrees of freedom. These results are reported and discussed as representative; indeed, similar accuracy can be achieved with different combination of polynomials order and number of elements as illustrated in the previous section. Fig. 4(b) shows the equilibrium path of the plate in terms of the non-dimensional load amplitude $\overline{F} = F(48a^2)/(\pi^2 Eb\tau^3)$ versus the non-dimensional transverse displacement $\overline{u}_3 = u_3/a$ evaluated at the load application point. The comparison of the present results with those of Ref. [10] evidences good agreement with small differences noticeable for higher load levels, being the dG solution less stiff. However, for both curves buckling starts in correspondence of very close load levels and the agreement is very good for the first part of the post-buckling behaviour. To show the evolution of the cantilever, slender plate kinematics with the applied load, some post-buckling configurations are shown in Fig. 4(c) for different equilibrium states, which correspond to the load levels $\overline{F} = 0.0$, 1.1, 1.72, 2.27, 2.75; the color map represents the normalized displacement magnitude $|\boldsymbol{u}|/a$.

Eventually, computation of stresses has been carried out and representative results are presented to complete the illustration of the method capabilities. They refer to the cantilevered slender plate modelled by the ED_{333} theory and solved with the same discretization described above, resulting in 1728 degrees of freedom. Fig. 5(a) and 5(b) show the through-the-thickness distributions of the normal stress σ_{11} and transverse shear stress σ_{13} at the reference domain points of coordinates $\xi_2 = b/2$ and $\xi_1 = a/3, a/2$ for different load amplitudes $\overline{F}$. It is worth to note that as expected the third-order model is able to inherently describe the quadratic distributions of the transverse shear stress.

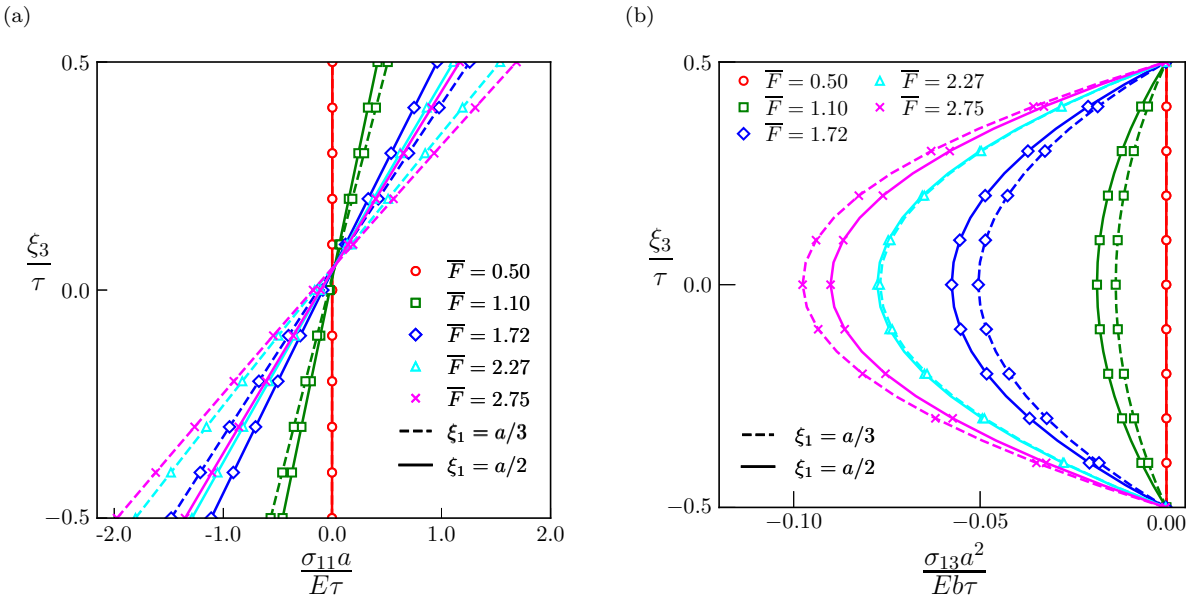

Figure 5: Through-the-thickness stress distributions at the reference domain points of coordinates $\xi_1 = a/3, a/2$ and $\xi_2 = b/2$ for the cantilevered slender plate with edge lengths $a = 300$ mm and $b = 60$ mm and thickness ratio $\tau/b = 0.1$. Stress distributions computed by the ED_{333} theory are plotted for different equilibrium states corresponding to the following compression loads $\overline{F} = 0.0, 1.1, 1.72, 2.27, 2.75$. (a) non-dimensional normal stress $\sigma_{11}a/E\tau$; (b) non-dimensional transverse shear stress $\sigma_{13}a^2/Eb\tau$.

4.3. Snap-back and snap-through of cylindrical shells

The third test focuses on the study of a cylindrical shell under loads and boundary conditions that result in a snap-back or snap-through behaviour of the structure. Fig. 6(a) shows the geometry, boundary conditions and loads of the cylindrical shell along with the orthogonal reference system $x_1x_2x_3$. Only a quarter of the structure is modelled for symmetry conditions. The mean surface of the shell is mapped as $x_{01} = R\sin(\xi_1)$, $x_{02} = \xi_2$ and $x_{03} = R\cos(\xi_1)$ where $\xi_1 \in [-\theta, 0]$, $\xi_2 \in [0, L]$, $L = 254$ mm, $R = 2540$ mm and $\theta = 0.1$ rad. Three different shell sections have been considered: *i*) a single-layer section of material M3 (see Table 1) and thickness $\tau = 6.35$mm, which is labeled as C1 case (thin shell); *ii*) a single-layer section of material M3 (see Table 1) and thickness $\tau = 12.7$mm, which is labeled as C2 case (moderately thick shell); *iii*) a three-layer section

with [0/90/0] layup of 4.233 mm thick plies having properties as M4 material in Table 1), which is labeled as C3 case. The boundary conditions of the first edge correspond to simply-supported, that is $u_{\xi_1} = u_{\xi_2} = u_{\xi_3} = 0$ at the points of coordinates $(-\theta,\ \xi_2,\ 0)$; the edge corresponding to $\xi_2 = 0$ is free, while the boundary conditions on the other two edges are used to enforce symmetry restraints, meaning $u_{\xi_1} = 0$ at the points of coordinates $(0,\ \xi_2,\ 0)$ and $u_{\xi_2} = 0$ at the points of coordinates $(\xi_1,\ L,\ 0)$. A transverse point load with amplitude F is applied at the coordinates $\xi_1 = 0, \xi_2 = L, \xi_3 = \tau/2$.

Fig. 6(b) shows the response of the analysed shells computed using the ED_{222} theory and a 2×2 mesh grid of elements with polynomial trial function order $p = 5$ resulting in 1296 degrees of freedom. Once again, it is remarked that the results obtained by this discretisation are representative and the same accuracy has been achieved with different combinations of mesh and elements approximation order. The curves of Fig. 6(b) plots the value of the load amplitude F as a function of the transverse displacement u_3 at the load application point. Figs. 6(c-l) show the shell configurations for selected equilibrium states. In particular, for the C1 section shell, Figs. 6(c-g) show the shell deformed shape at the load levels $F = 0.283,\ -0.315,\ 0.185,\ 1.576,\ 3.0\,[\mathrm{kN}]$, whereas Figs. 6(h-l) illustrate the behaviour of the C3 section shell showing its configurations at $F = 1.043,\ 1.661,\ 0.861,\ 1.803,\ 3.045\,[\mathrm{kN}]$. The shell configurations of Figs 6(c-l) are supplemented by the displacement magnitude $|\boldsymbol{u}|$ maps, which refer to the colorbar of Fig. 6(m). Clearly, snap-back or snap-through behaviour occurs depending on the shell thickness ratio and the comparison of the present results with those available from Refs. [11], [70] and [71] shows good agreement for both isotropic and multilayered cases.

Fig. 7 illustrates the through-the-thickness distribution of representative stress components computed for the C3 section shell at the point $\xi_1 = \theta/4$ and $\xi_2 = L/4$. These are com-

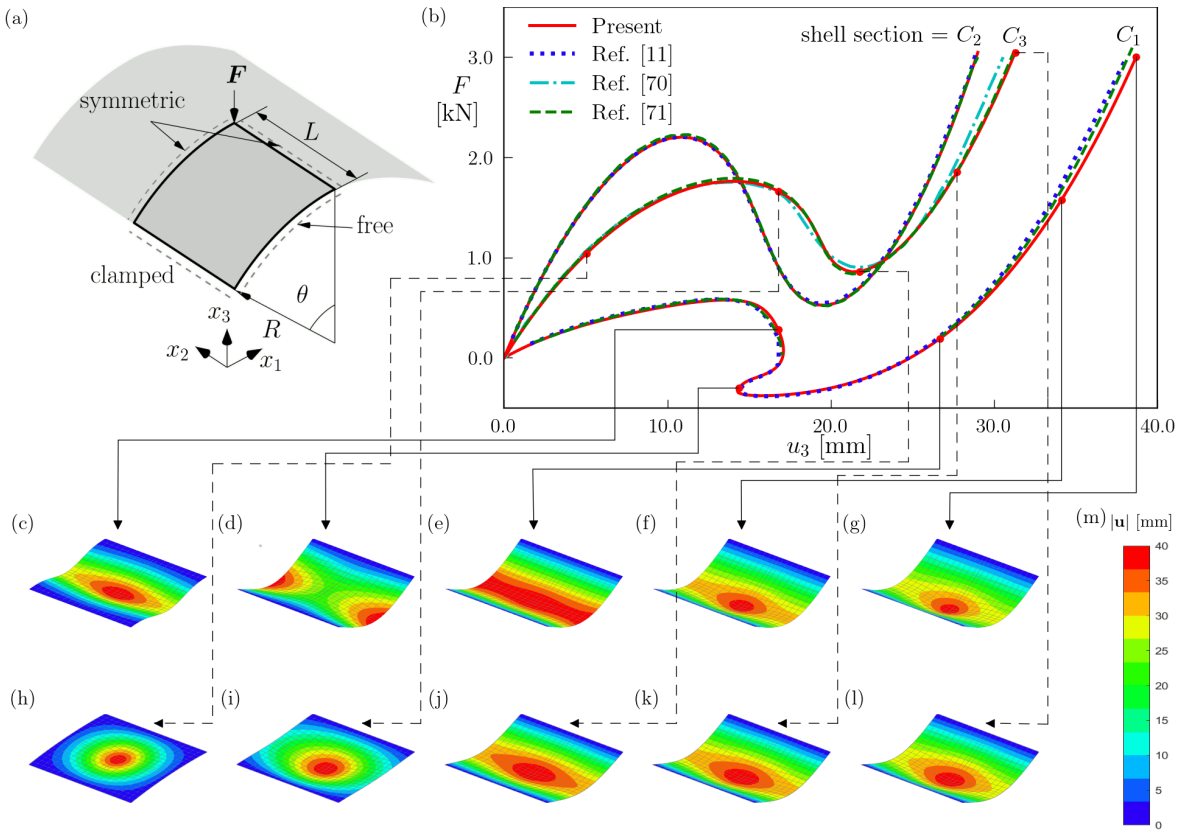

Figure 6: Cylindrical shells with snap-back and snap-through behaviour. (a) Geometry, boundary conditions and applied load: $L = 254$ mm, $R = 2540$ mm and $\theta = 0.1$ rad. (b) Nonlinear equilibrium path in terms of load amplitude F versus the transverse displacement u_3 at the load application point for the three examined shell sections: *i)* a 6.35mm thin homogeneous section of material M_3, labeled as C_1, *ii)* a 12.7mm moderately thick homogeneous section of material M_3, labeled as C_2, and *iii)* a 12.7mm thick layered section with [0/90/0] layup of M_4 material, equal thickness plies, labeled as C_3. M_3 and M_4 material properties are given in Table 1. Results are obtained using the ED_{222} theory solved by a 2×2 mesh grid of elements with polynomial trial function order $p = 5$. (c-g) show the C_1 section shell configurations for different equilibrium states corresponding to $F = 0.283, -0.315, 0.185, 1.576, 3.0$ [kN]. (h-l) show the C_3 section shell configurations for different equilibrium states corresponding to $F = 1.043, 1.661, 0.861\, 1.803, 3.045$ [kN]. The color maps represent the displacement magnitude $|\boldsymbol{u}|$ and refer to the colorbar in (m).

puted for the equilibrium states corresponding to $F = 1.043,\ 1.661,\ 0.861,\ 1.803,\ 3.045$ [kN] by using both the ED_{222} and ED_{333} models with the same domain discretization described above. As expected, the results shows that both the models are able to capture the in-plane stress distribution with the same accuracy level as evidenced by Fig. 7(a) where the σ_{11} curves are almost coincident for the two theories employed. As regard the transverse

shear stresses, Fig. 7(b) shows the σ_{13} stress results. They indicate that the ED_{222} model is not able to provide reliable shear stress distributions, e.g. the traction-free surface condition is not ensured; on the other hand the ED_{333} theory generally give physically reliable and sound distributions.

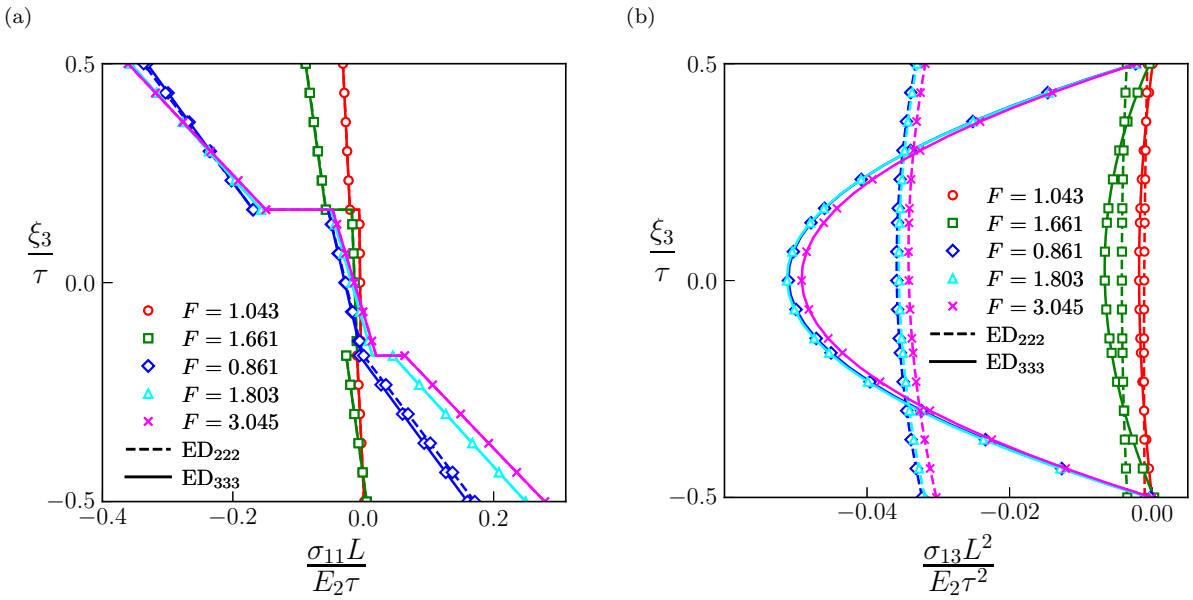

Figure 7: Through-the-thickness stress distributions for the pinched cylindrical shell with radius $R = 2540$ mm, central half-angle $\theta = 0.1$ rad, half-length $L = 254$ mm and [0/90/0] layup with 4.233 mm thick plies of M4 material (see Table 1). Stress distributions at the reference domain points of coordinates $\xi_1 = \theta/4$ and $\xi_2 = L/4$ are plotted for different equilibrium states corresponding to the load amplitudes $F = 1.043, 1.661, 0.861, 1.803, 3.045$ [kN]. (a) non-dimensional normal stress $\sigma_{11}L/E_2\tau$; (b) non-dimensional transverse shear stress $\sigma_{13}L^2/E_2\tau^2$, being E_2 the M4 material transverse Young's module and τ the shell thickness.

These results illustrate the capabilities of the proposed method to deal with complex nonlinear behaviour of shells.

4.4. NURBS-based laminated shell

In the last test, a generally-curved shell is considered, whose geometry is shown in Fig. 8(a-c) being $L = 600$ mm, $H = 500$ mm and $D = 50$ mm.

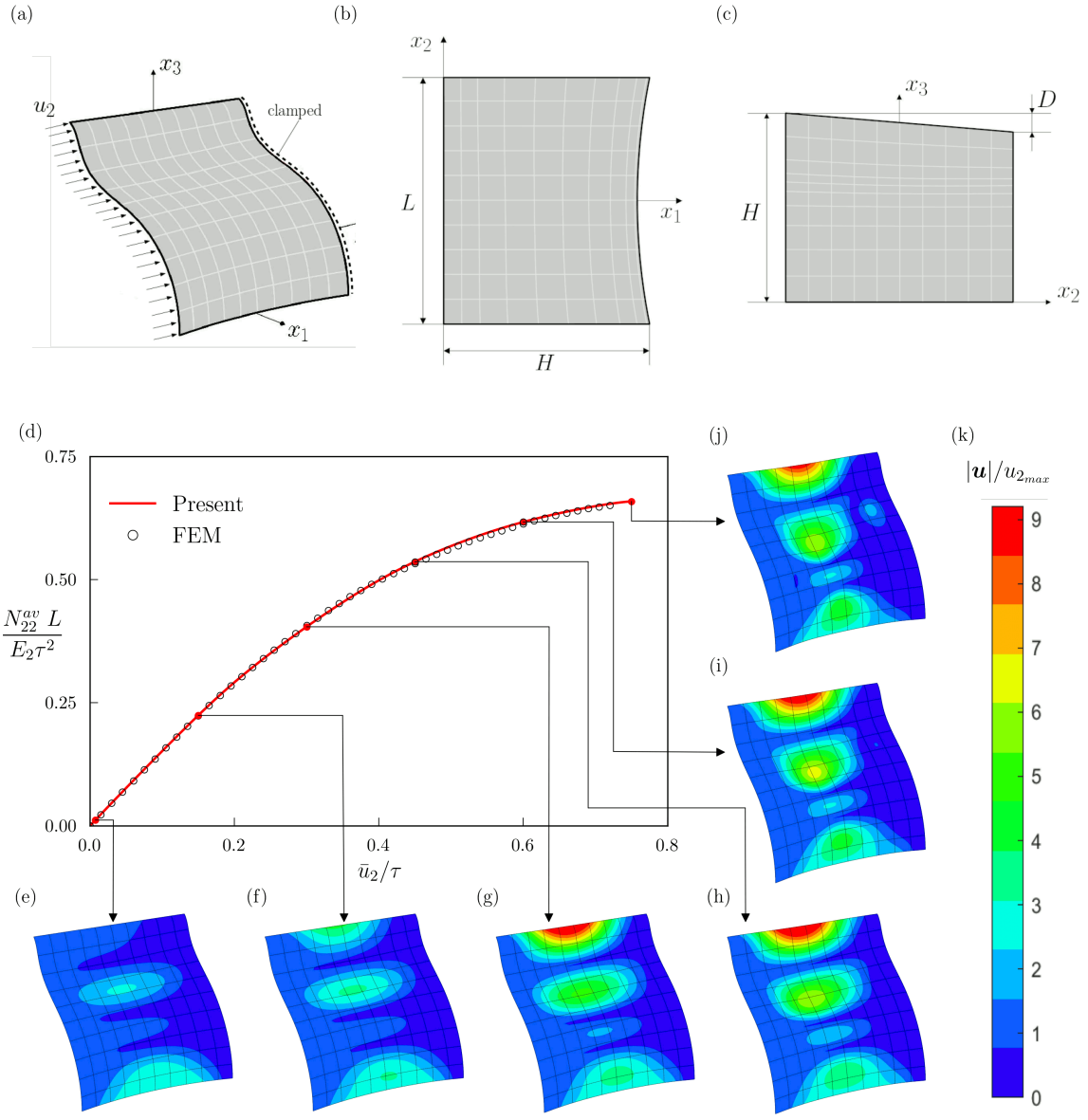

Figure 8: NURBS-based shell undergoing compression loading. (a-c) Geometry and loading conditions of the shell: $L = 600$ mm, $H = 500$ mm and $D = 50$ mm; NURBS data to replicate the geometry are given in Ref. [60]. (d) Equilibrium path in terms of the average x_2-directed edge force resultant per unit length N_{22}^{av} versus the applied edge displacement u_2. Color maps of the non-dimensional displacement vector magnitude $|\boldsymbol{u}|/u_{2_{max}}$ at the reference surface points are also shown at the following percentage levels of the loading: (e) 1%, (f) 20%, (g) 40%, (h) 60%, (i) 80%, (j) 100%; they refer to the colorbar shown in (k) where $u_{2_{max}}$ is the maximum loading amplitude.

The shell geometry is described via NURBS functions and for its data, including the

coordinates of the control points, the degree of the basis functions and the knot vectors, the reader is referred to [60]. The shell section is a four layers laminate with 1 mm thick plies of material M4 (see Table 1) and $[0, 30, 60, 90]$ layup. The shell is clamped on the edge corresponding to $\xi_2 = 1$ and it is subjected on the opposite edge to an uniform, compression displacement u_2 directed along x_2. The shell is modelled with the ED_{222} theory and the simulation has been carried out using a 10×10 grid of elements with polynomial order $p = 4$ resulting in 22500 degrees of freedom.

Fig. 8(d) shows the shell load-end displacement curve in terms of the average x_2-directed edge force resultant per unit length, namely N_{22}^{av}, versus the applied edge displacement u_2. The curve is compared with that obtained by finite elements using the Abaqus® software [72] evidencing very good agreement. Additionally, Fig. 8(e-j) show the contour maps of the displacement vector magnitude $|\boldsymbol{u}|$ of the reference surface points at the loading steps corresponding to 1%, 20%, 40%, 60%, 80% and 100% of the maximum applied compression displacement $u_{2_{max}}$. It is evidenced the complex behaviour of the investigated shell which experiences coupling effects related to its geometry and layup. It is worth to note that a thin shell has been used in this test. This allows to consider accurate the finite element solution obtained with the first order shear deformation theory whereas a second order theory has been employed in the dG modelization, so as to validate the proposed refined approach in the framework of such a complex shell geometry.

In conclusion, the favourable comparison of the presented solutions with the literature and finite elements results validates the proposed approach whose accuracy can be tuned acting both on the employed number of mesh elements or on the order of the elements polynomial approximation.

5. Conclusions

This work presents a novel pure penalty discontinuous Galerkin method for the geometrically nonlinear static analysis of multilayered plates and shells.

In the context of a total Lagrangian approach, it allows to implement refined equivalent single-layer shell theories with generality of the through-the-thickness resolution. The corresponding governing equations are obtained by the principle of virtual works and, for the first time, their discretised form is inferred by a discontinuous Galerkin approach resting on the pure penalty formulation. Based on Legendre polynomial expansion of the primary variables, high-order elements are developed. The resulting nonlinear algebraic system is solved with a Newton-Raphson arc-length scheme.

A set of test cases is carried outto validate the proposed approach and assess its features, focusing on nonlinear bending and post-buckling response of plates, the snap-back and snap-through of shells, and the analysis of complex shell geometries. The tests prove the ability of the method to deal with complex nonlinear behaviour of plates and shells.

Indeed, the obtained results reveal very good agreement with those from the literature or from finite element analyses. The convergence studies show that the method is effective with respect to the element order, which entails good accuracy with reduced computational effort especially for high-order theory modelling. From this point of view, it is observed that the use of the pure penalty approach in the formulation requires to compute the elements interface boundary integrals only once, thus saving computational time during the iterative solution scheme.

On the other hand, it is observed that the method tends to provide less stiff response for high loading levels. This behaviour might be induced by the pure penalty approach, which enforces in a weak sense the kinematical compatibility at the element interfaces

without ensuring internal forces equilibrium. This aspect deserves further investigations.

Overall, the proposed pure penalty discontinuous Galerkin method can be an alternative and useful mean for the nonlinear analysis of multilayered plates and shells modelled with high-order, refined two-dimensional theories. The class of configurations that can be analysed is relatively wide. Future development should be directed towards the extension of the method to handle typical features found in practical applications such as nonlinear material behaviour, nonlinear dynamics, damage.

6. Acknowledgements

The authors would like to acknowledge the DEVISU project, supported by the Ministero dell'Istruzione, dell'Università della Ricerca research, funding programme PRIN 2017.

References

[1] T. V. Kármán, Festigkeitsprobleme im maschinenbau, in: Mechanik, Springer, 1907, pp. 311–385.

[2] V. G. Kirchhoff, Über das gleichgewicht und die bewegung einer elastischen scheibe, Journal fur die reine und angewandte Mathematik 40 (1850) 51–88.

[3] E. Reissner, The effect of transverse shear deformation on the bending of elastic plates, ASME Journal of Applied Mechanics 12 (2) (1945) 69–77.

[4] R. Mindlin, Influence of rotatory inertia and shear on flexural motions of isotropic, elastic plates, ASME Journal of Applied Mechanics 18 (1) (1951) 31–38.

[5] C.-Y. Chia, Nonlinear analysis of plates, McGraw-Hill International Book Company, 1980.

[6] E. Carrera, Theories and finite elements for multilayered, anisotropic, composite plates and shells, Archives of Computational Methods in Engineering 9 (2) (2002) 87–140.

[7] E. Carrera, Theories and finite elements for multilayered plates and shells: a unified compact formulation with numerical assessment and benchmarking, Archives of Computational Methods in Engineering 10 (3) (2003) 215–296.

[8] E. Carrera, A. Pagani, D. Giusa, R. Augello, Nonlinear analysis of thin-walled beams with highly deformable sections, International Journal of Non-Linear Mechanics 128 (2021) 103613.

[9] E. Carrera, A. Pagani, R. Augello, B. Wu, Popular benchmarks of nonlinear shell analysis solved by 1d and 2d CUF-based finite elements, Mechanics of Advanced Materials and Structures 27 (13) (2020) 1098–1109.

[10] B. Wu, A. Pagani, M. Filippi, W. Chen, E. Carrera, Large-deflection and post-buckling analyses of isotropic rectangular plates by Carrera Unified Formulation, International Journal of Non-Linear Mechanics 116 (2019) 18–31.

[11] B. Wu, A. Pagani, W. Chen, E. Carrera, Geometrically nonlinear refined shell theories by Carrera Unified Formulation, Mechanics of Advanced Materials and Structures 28 (16) (2021) 1721–1741.

[12] A. Pagani, R. Azzara, B. Wu, E. Carrera, Effect of different geometrically nonlinear strain measures on the static nonlinear response of isotropic and composite shells with constant curvature, International Journal of Mechanical Sciences 209 (2021) 106713.

[13] A. Milazzo, V. Oliveri, Post-buckling analysis of cracked multilayered composite plates by pb-2 Rayleigh–Ritz method, Composite Structures 132 (2015) 75–86.

[14] A. Milazzo, V. Oliveri, Buckling and postbuckling of stiffened composite panels with cracks and delaminations by Ritz approach, AIAA Journal 55 (3) (2017) 965–980.

[15] V. Oliveri, A. Milazzo, A Rayleigh-Ritz approach for postbuckling analysis of variable angle tow composite stiffened panels, Computers & Structures 196 (2018) 263–276.

[16] A. Milazzo, I. Benedetti, V. Gulizzi, An extended Ritz formulation for buckling and post-buckling analysis of cracked multilayered plates, Composite Structures 201 (2018) 980–994.

[17] V. Gulizzi, V. Oliveri, A. Milazzo, Buckling and post-buckling analysis of cracked stiffened panels via an X-Ritz method, Aerospace Science and Technology 86 (2019) 268–282.

[18] A. Milazzo, G. Guarino, V. Gulizzi, Buckling and post-buckling of variable stiffness plates with cutouts by a single-domain Ritz method, Thin-Walled Structures 182 (2023) 110282.

[19] R. A. Arcinega, P. B. Gonçalves, J. N. Reddy, Buckling and postbuckling analysis of laminated cylindrical shells using the thrd-order shear deformation theory, International Journal of Structural Stability and Dynamics 04 (03) (2004) 293–312.

[20] H. Ovesy, M. Taghizadeh, M. Kharazi, Post-buckling analysis of composite plates containing embedded delaminations with arbitrary shape by using higher order shear deformation theory, Composite Structures 94 (3) (2012) 1243–1249.

[21] J. Lin, H. Naceur, A. Laksimi, D. Coutellier, On the implementation of a nonlinear shell-based sph method for thin multilayered structures, Composite Structures 108 (2014) 905–914.

[22] M. Fouaidi, A. Hamdaoui, M. Jamal, B. Braikat, A high order mesh-free method for buckling and post-buckling analysis of shells, Engineering Analysis with Boundary Elements 99 (2019) 89–99.

[23] S. Hosseini, G. Rahimi, D. Shahgholian-Ghahfarokhi, A meshless collocation method on nonlinear analysis of functionally graded hyperelastic plates using radial basis function, ZAMM - Journal of Applied Mathematics and Mechanics / Zeitschrift für Angewandte Mathematik und Mechanik 102 (2) (2022) e202100216.

[24] C. Roque, J. Grasa, Geometrically nonlinear analysis of laminated composite plates using rbf-ps meshless method, Composite Structures 267 (2021) 113830.

[25] P. Antolin, A. Buffa, L. Coradello, A hierarchical approach to the a posteriori error estimation of isogeometric Kirchhoff plates and Kirchhoff–Love shells, Computer Methods in Applied Mechanics and Engineering 363 (2020) 112919.

[26] A. Patton, P. Antolin, J.-E. Dufour, J. Kiendl, A. Reali, Accurate equilibrium-based interlaminar stress recovery for isogeometric laminated composite Kirchhoff plates, Composite Structures 256 (2021) 112976.

[27] T. N. Nguyen, S. Lee, P.-C. Nguyen, H. Nguyen-Xuan, J. Lee, Geometrically nonlinear postbuckling behavior of imperfect FG-CNTRC shells under axial compression using isogeometric analysis, European Journal of Mechanics-A/Solids 84 (2020) 104066.

[28] G. Radenković, A. Borković, B. Marussig, Nonlinear static isogeometric analysis of

arbitrarily curved Kirchhoff-Love shells, International Journal of Mechanical Sciences 192 (2021) 106143.

[29] Y. Guo, Z. Zou, M. Ruess, Isogeometric multi-patch analyses for mixed thin shells in the framework of non-linear elasticity, Computer Methods in Applied Mechanics and Engineering 380 (2021).

[30] R. Zhang, G. Zhao, W. Wang, X. Du, Large deformation frictional contact formulations for isogeometric Kirchhoff–Love shell, International Journal of Mechanical Sciences 249 (2023).

[31] A. Patton, P. Antolin, J. Kiendl, A. Reali, Efficient equilibrium-based stress recovery for isogeometric laminated curved structures, Composite Structures 272 (2021) 113975.

[32] C. H. Thai, H. Nguyen-Xuan, S. P. A. Bordas, N. Nguyen-Thanh, T. Rabczuk, Isogeometric analysis of laminated composite plates using the higher-order shear deformation theory, Mechanics of Advanced Materials and Structures 22 (6) (2015) 451–469.

[33] Y. Kiani, M. Mirzaei, Isogeometric thermal postbuckling of FG-GPLRC laminated plates, Steel and Composite Structures 32 (2019) 821–832.

[34] D. N. Arnold, F. Brezzi, Cockburn, B., L. D. Marini, Unified analysis of discontinuous Galerkin methods for elliptic problems, SIAM Journal on Numerical Analysis 39 (5) (2002) 1749–1779.

[35] B. Rivière, S. Shaw, M. F. Wheeler, J. Whiteman, Discontinuous Galerkin finite element methods for linear elasticity and quasistatic linear viscoelasticity, Numerische Mathematik 95 (2003) 347–376.

[36] A. Ten Eyck, A. Lew, Discontinuous Galerkin methods for non-linear elasticity, International Journal for Numerical Methods in Engineering 67 (9) (2006) 1204–1243.

[37] R. An, X. Huang, A compact c0 discontinuous Galerkin method for Kirchhoff plates, Numerical Methods for Partial Differential Equations 31 (4) (2015) 1265–1287.

[38] X. Huang, J. Huang, A superconvergent C0 discontinuous Galerkin method for Kirchhoff plates: Error estimates, hybridization and postprocessing, Journal of Scientific Computing 69 (3) (2016) 1251–1278.

[39] J. Cui, Y. Zhang, A new analysis of discontinuous Galerkin methods for a fourth order variational inequality, Computer Methods in Applied Mechanics and Engineering 351 (2019) 531–547.

[40] P. Bösing, C. Carstensen, Weakly over-penalized discontinuous Galerkin schemes for Reissner–Mindlin plates without the shear variable, Numerische Mathematik 130 (3) (2015) 395–423.

[41] P. Bösing, C. Carstensen, Discontinuous Galerkin with weakly over-penalized techniques for Reissner–Mindlin plates, Journal of Scientific Computing 64 (2) (2015) 401–424.

[42] L. Mu, J. Wang, X. Ye, A weak Galerkin method for the Reissner–Mindlin plate in primary form, Journal of Scientific Computing 75 (2) (2018) 782 – 802.

[43] L. Noels, R. Radovitzky, A new discontinuous Galerkin method for Kirchhoff–Love shells, Computer Methods in Applied Mechanics and Engineering 197 (33-40) (2008) 2901–2929.

[44] S. Zhang, Analysis of a discontinuous Galerkin method for the bending problem of Koiter shell, Numerische Mathematik 133 (2) (2016) 333 – 370.

[45] Y. Xia, H. Wang, G. Zheng, G. Shen, P. Hu, Discontinuous Galerkin isogeometric analysis with peridynamic model for crack simulation of shell structure, Computer Methods in Applied Mechanics and Engineering 398 (2022).

[46] A. Bonito, R. H. Nochetto, D. Ntogkas, Discontinuous Galerkin approach to large bending deformation of a bilayer plate with isometry constraint, Journal of Computational Physics 423 (2020) 109785.

[47] A. Bonito, R. Nochetto, D. Ntogkas, DG approach to large bending plate deformations with isometry constraint, Mathematical Models and Methods in Applied Sciences 31 (1) (2021) 133–175.

[48] S. Bartels, A. Bonito, P. Hornung, Modeling and simulation of thin sheet folding, Interfaces and Free Boundaries 24 (4) (2022) 459–485.

[49] L. Noels, A discontinuous Galerkin formulation of non-linear Kirchhoff–Love shells, International journal for numerical methods in engineering 78 (3) (2009) 296–323.

[50] L. Noels, A one-field discontinuous Galerkin formulation of non-linear Kirchhoff-Love shells, International Journal of Material Forming 2 (SUPPL. 1) (2009) 877 – 880.

[51] G. Becker, L. Noels, A full-discontinuous Galerkin formulation of nonlinear Kirchhoff-Love shells: Elasto-plastic finite deformations, parallel computation, and fracture applications, International Journal for Numerical Methods in Engineering 93 (1) (2013) 80–117.

[52] B. L. Talamini, R. Radovitzky, A discontinuous Galerkin method for nonlinear shear-flexible shells, Computer methods in applied mechanics and engineering 303 (2016) 128–162.

[53] B. L. Talamini, R. Radovitzky, A parallel discontinuous Galerkin/cohesive-zone computational framework for the simulation of fracture in shear-flexible shells, Computer Methods in Applied Mechanics and Engineering 317 (2017) 480 – 506.

[54] D. Versino, H. M. Mourad, T. O. Williams, A global-local discontinuous Galerkin shell finite element for small-deformation analysis of multi-layered composites, Computer Methods in Applied Mechanics and Engineering 271 (2014) 269 – 295.

[55] D. Versino, H. M. Mourad, T. O. Williams, F. L. Addessio, A global–local discontinuous Galerkin finite element for finite-deformation analysis of multilayered shells, Computer Methods in Applied Mechanics and Engineering 283 (2015) 1401–1424.

[56] V. Gulizzi, I. Benedetti, A. Milazzo, An implicit mesh discontinuous Galerkin formulation for higher-order plate theories, Mechanics of Advanced Materials and Structures 27 (17) (2020) 1494–1508.

[57] V. Gulizzi, I. Benedetti, A. Milazzo, A high-resolution layer-wise discontinuous Galerkin formulation for multilayered composite plates, Composite Structures (2020) 112137.

[58] I. Benedetti, V. Gulizzi, A. Milazzo, Layer-wise discontinuous Galerkin methods for piezoelectric laminates, Modelling 1 (2) (2020) 198–214.

[59] G. Guarino, A. Milazzo, V. Gulizzi, Equivalent-single-layer discontinuous Galerkin

methods for static analysis of multilayered shells, Applied Mathematical Modelling 98 (2021) 701–721.

[60] G. Guarino, V. Gulizzi, A. Milazzo, High-fidelity analysis of multilayered shells with cut-outs via the discontinuous Galerkin method, Composite Structures 276 (2021) 114499.

[61] G. Guarino, V. Gulizzi, A. Milazzo, Accurate multilayered shell buckling analysis via the implicit-mesh discontinuous galerkin method, AIAA Journal 60 (12) (2022) 6854 – 6868.

[62] P. G. Ciarlet, An introduction to differential geometry with applications to elasticity, Journal of Elasticity 78 (1-3) (2005) 1–215.

[63] I. Babuška, The finite element method with penalty, Mathematics of computation 27 (122) (1973) 221–228.

[64] I. Babuška, M. Zlámal, Nonconforming elements in the finite element method with penalty, SIAM Journal on Numerical Analysis 10 (5) (1973) 863–875.

[65] P. R. Bösing, A. L. Madureira, I. Mozolevski, A new interior penalty discontinuous Galerkin method for the Reissner–Mindlin model, Mathematical Models and Methods in Applied Sciences 20 (08) (2010) 1343–1361.

[66] P. Castillo, Performance of discontinuous Galerkin methods for elliptic PDEs, SIAM Journal on Scientific Computing 24 (2) (2002) 524–547.

[67] M. A. Crisfield, A fast incremental/iterative solution procedure that handles "snap-through", in: Computational methods in nonlinear structural and solid mechanics, Elsevier, 1981, pp. 55–62.

[68] M. Crisfield, An arc-length method including line searches and accelerations, International Journal for Numerical Methods in Engineering 19 (9) (1983) 1269–1289.

[69] G. Turvey, M. Osman, Elastic large deflection analysis of isotropic rectangular Mindlin plates, International Journal of Mechanical Sciences 32 (4) (1990) 315–328.

[70] E. Carrera, A. Pagani, R. Azzara, R. Augello, Vibration of metallic and composite shells in geometrical nonlinear equilibrium states, Thin-Walled Structures 157 (2020) 107131.

[71] K. Sze, X. Liu, S. Lo, Popular benchmark problems for geometric nonlinear analysis of shells, Finite Elements in Analysis and Design 40 (11) (2004) 1551–1569.

[72] M. Smith, ABAQUS 6.14 Documentation, Dassault Systèmes, 2014, Providence, RI, USA.

Appendix A. Layer stiffness matrix

The layer stiffness matrix in the orthotropic material reference system is built as

$$\widetilde{\boldsymbol{c}}^{\langle \ell \rangle} = \begin{bmatrix} \frac{1}{E_1} & -\frac{\nu_{21}}{E_2} & -\frac{\nu_{31}}{E_3} & 0 & 0 & 0 \\ -\frac{\nu_{12}}{E_1} & \frac{1}{E_2} & -\frac{\nu_{32}}{E_3} & 0 & 0 & 0 \\ -\frac{\nu_{13}}{E_1} & -\frac{\nu_{23}}{E_2} & \frac{1}{E_3} & 0 & 0 & 0 \\ 0 & 0 & 0 & \frac{1}{G_{23}} & 0 & 0 \\ 0 & 0 & 0 & 0 & \frac{1}{G_{31}} & 0 \\ 0 & 0 & 0 & 0 & 0 & \frac{1}{G_{12}} \end{bmatrix}^{-1} \tag{A.1}$$

where E_r, ν_{rs} and G_{rs} are the orthotropic material Young' moduli, Poisson' coefficients and shear moduli, respectively.

In turn, the layer stiffness matrix in the orthogonal reference system $x_1x_2x_3$, namely $\boldsymbol{c}^{\langle \ell \rangle}$, is obtained via Eq. (17) by using the following transformation matrix

$$\boldsymbol{T} = \begin{bmatrix} \lambda_{11}^2 & \lambda_{12}^2 & \lambda_{13}^2 & 2\lambda_{12}\lambda_{13} & 2\lambda_{11}\lambda_{13} & 2\lambda_{11}\lambda_{12} \\ \lambda_{21}^2 & \lambda_{22}^2 & \lambda_{23}^2 & 2\lambda_{22}\lambda_{23} & 2\lambda_{21}\lambda_{23} & 2\lambda_{21}\lambda_{22} \\ \lambda_{31}^2 & \lambda_{32}^2 & \lambda_{33}^2 & 2\lambda_{32}\lambda_{33} & 2\lambda_{31}\lambda_{33} & 2\lambda_{31}\lambda_{32} \\ \lambda_{21}\lambda_{31} & \lambda_{22}\lambda_{32} & \lambda_{23}\lambda_{33} & \lambda_{22}\lambda_{33}+\lambda_{23}\lambda_{32} & \lambda_{21}\lambda_{33}+\lambda_{23}\lambda_{31} & \lambda_{21}\lambda_{32}+\lambda_{22}\lambda_{31} \\ \lambda_{11}\lambda_{31} & \lambda_{12}\lambda_{32} & \lambda_{13}\lambda_{33} & \lambda_{12}\lambda_{33}+\lambda_{13}\lambda_{32} & \lambda_{11}\lambda_{33}+\lambda_{13}\lambda_{31} & \lambda_{11}\lambda_{32}+\lambda_{12}\lambda_{31} \\ \lambda_{11}\lambda_{21} & \lambda_{12}\lambda_{22} & \lambda_{13}\lambda_{23} & \lambda_{12}\lambda_{23}+\lambda_{13}\lambda_{22} & \lambda_{11}\lambda_{23}+\lambda_{13}\lambda_{21} & \lambda_{11}\lambda_{22}+\lambda_{12}\lambda_{21} \end{bmatrix} \tag{A.2}$$

where λ_{ij} is the directional cosine of $\boldsymbol{m}_i$ on x_j.

Appendix B. Tangent stiffness matrix

The stiffness matrix $\boldsymbol{K}$ appearing in the resolving system is a function of $\boldsymbol{X}$ and can be decomposed into three kinds of contributes, namely $\boldsymbol{K} = \boldsymbol{K}_I + \boldsymbol{K}_{II} + \boldsymbol{K}_{III}$, which originates from the work of internal forces, the enforcement of the continuity of the solution across the elements and the enforcement of the problem essential boundary conditions, respectively. Since adopting a Pure Penalty formulation the contributions $\boldsymbol{K}_{II}$ and $\boldsymbol{K}_{III}$ do not depend on $\boldsymbol{X}$. Therefore, the tangent stiffness matrix $\boldsymbol{K}_T$ associated with the stiffness matrix $\boldsymbol{K}$ is expressed as

$$\boldsymbol{K}_T = \frac{\partial(\boldsymbol{K}_I\boldsymbol{X})}{\partial \boldsymbol{X}} + \boldsymbol{K}_{II} + \boldsymbol{K}_{III} = \boldsymbol{K}_I^J + \boldsymbol{K}_{II} + \boldsymbol{K}_{III}. \tag{B.1}$$

The term $\boldsymbol{K}_I^J = \partial(\boldsymbol{K}_I \boldsymbol{X})/\partial \boldsymbol{X}$ stems from the variation of the virtual work of the internal forces

$$\delta(\delta L_{int}) = \sum_{\ell=1}^{N_\ell} \int_{V^{\langle \ell \rangle}} \delta(\delta \boldsymbol{\gamma}^{\mathrm{T}} \boldsymbol{\sigma}^{\langle \ell \rangle}) \mathrm{d}V \tag{B.2}$$

which, after some manipulations, accounting for Eqs. (11) and for the constitutive equations, Eq. (B.2) is written as

$$\delta(\delta L_{int}) = \sum_{\ell=1}^{N_\ell} \int_{V^{\langle \ell \rangle}} \frac{\partial \delta \boldsymbol{u}}{\partial x_i}^{\mathrm{T}} \boldsymbol{C}_{ij}^J \frac{\partial \delta \boldsymbol{u}}{\partial x_j} \mathrm{d}V \tag{B.3}$$

where

$$\boldsymbol{C}_{ij}^J = (\boldsymbol{I}_i + \boldsymbol{W}_i)^{\mathrm{T}} \boldsymbol{c} (\boldsymbol{I}_j + \boldsymbol{W}_j) + \sigma_{ij}^{\langle \ell \rangle} \boldsymbol{I}_d, \tag{B.4}$$

being $\boldsymbol{I}_d$ the 3×3 identity matrix. Using Eq. (13) and integrating over the thickness, Eq. (B.3) becomes

$$\delta(\delta L_{int}) = \int_{\Omega_\xi} \left[\frac{\partial \delta \boldsymbol{U}^{\mathrm{T}}}{\partial \xi_\alpha} \left(\boldsymbol{Q}_{\alpha\beta}^J \frac{\partial \delta \boldsymbol{U}}{\partial \xi_\beta} + \boldsymbol{R}_{\alpha 3}^J \delta \boldsymbol{U} \right) + \delta \boldsymbol{U}^{\mathrm{T}} \left(\boldsymbol{R}_{3\alpha}^J \frac{\partial \delta \boldsymbol{U}}{\partial \xi_\alpha} + \boldsymbol{S}_{33}^J \delta \boldsymbol{U} \right) \right] \mathrm{d}\Omega_\xi, \tag{B.5}$$

where the generalized tangent stiffness matrices are introduced as

$$\boldsymbol{Q}_{\alpha\beta}^J \equiv \sum_{\ell=1}^{N_\ell} \int_{\xi_{3b}^{\langle \ell \rangle}}^{\xi_{3t}^{\langle \ell \rangle}} \boldsymbol{D}_{\alpha i}^{\mathrm{T}} \boldsymbol{C}_{ij}^J \boldsymbol{D}_{\beta j} \sqrt{g} \, \mathrm{d}\xi_3, \tag{B.6a}$$

$$\boldsymbol{R}_{\alpha 3}^J \equiv \sum_{\ell=1}^{N_\ell} \int_{\xi_{3b}^{\langle \ell \rangle}}^{\xi_{3t}^{\langle \ell \rangle}} \boldsymbol{D}_{\alpha i}^{\mathrm{T}} \boldsymbol{C}_{ij}^J \boldsymbol{D}_{0 j} \sqrt{g} \, \mathrm{d}\xi_3, \tag{B.6b}$$

$$\boldsymbol{R}_{3\alpha}^J \equiv \sum_{\ell=1}^{N_\ell} \int_{\xi_{3b}^{\langle \ell \rangle}}^{\xi_{3t}^{\langle \ell \rangle}} \boldsymbol{D}_{0 i}^{\mathrm{T}} \boldsymbol{C}_{ij}^J \boldsymbol{D}_{\alpha j} \sqrt{g} \, \mathrm{d}\xi_3 \tag{B.6c}$$

$$\boldsymbol{S}_{33}^J \equiv \sum_{\ell=1}^{N_\ell} \int_{\xi_{3b}^{\langle \ell \rangle}}^{\xi_{3t}^{\langle \ell \rangle}} \boldsymbol{D}_{0 i}^{\mathrm{T}} \boldsymbol{C}_{ij}^J \boldsymbol{D}_{0 j} \sqrt{g} \, \mathrm{d}\xi_3. \tag{B.6d}$$

Accordingly to Eq. (B.5) the e-th element provides a contribution to $\boldsymbol{K}_I^J$ given by

$$\boldsymbol{K}_I^e = \int_{\Omega_\xi^e} \left[\frac{\partial \boldsymbol{P}^{e\mathrm{T}}}{\partial \xi_\alpha} \left(\boldsymbol{Q}_{\alpha\beta}^J \frac{\partial \boldsymbol{P}^e}{\partial \xi_\beta} + \boldsymbol{R}_{\alpha 3}^J \boldsymbol{P}^e \right) + \boldsymbol{P}^{e\mathrm{T}} \left(\boldsymbol{R}_{3\alpha}^J \frac{\partial \boldsymbol{P}^e}{\partial \xi_\alpha} + \boldsymbol{S}_{33}^J \boldsymbol{P}^e \right) \right] \mathrm{d}\Omega_\xi, \qquad \text{(B.7)}$$

that sums to the row and columns of the tangent stiffness matrix associated with the degrees of freedom of the element.